



Rapid Stellar and Binary Population Synthesis with COMPAS

Team COMPAS¹⁶,

Jeff Riley^{1,2} , Poojan Agrawal^{2,3} , Jim W. Barrett⁴ , Kristan N. K. Boyett⁵ , Floor S. Broekgaarden⁶ ,
 Debatri Chattopadhyay^{2,3} , Sebastian M. Gaebel⁷ , Fabian Gittins⁸ , Ryosuke Hirai^{1,2} , George Howitt^{2,9} ,
 Stephen Justham^{10,11,12} , Lokesh Khandelwal¹⁰ , Floris Kummer¹⁰ , Mike Y. M. Lau^{1,2} , Ilya Mandel^{1,2,4} ,
 Selma E. de Mink^{6,10,12} , Coenraad Neijssel^{2,4} , Tim Riley^{1,2} , Lieke van Son^{6,10,12} , Simon Stevenson^{2,3} ,
 Alejandro Vigna-Gómez^{13,14} , Serena Vinciguerra¹⁰ , Tom Wagg^{6,12,15} , and Reinhold Willcox^{1,2} 

¹ School of Physics and Astronomy, Monash University, Clayton, Victoria 3800, Australia; jeff.riley@monash.edu, ilya.mandel@monash.edu² OzGrav, Australian Research Council Centre of Excellence for Gravitational Wave Discovery, Australia; spstevenson@swin.edu.au³ Centre for Astrophysics and Supercomputing, Swinburne University of Technology, Hawthorn, VIC 3122, Australia⁴ Institute of Gravitational Wave Astronomy and School of Physics and Astronomy, University of Birmingham, Birmingham B15 2TT, UK⁵ Department of Physics, University of Oxford, Denys Wilkinson Building, Keble Road, Oxford OX1 3RH, UK⁶ Center for Astrophysics | Harvard & Smithsonian, 60 Garden St., Cambridge, MA 02138, USA; floor.broekgaarden@cfa.harvard.edu⁷ Max Planck Institute for Gravitational Physics (Albert Einstein Institute), Callinstrasse 38, D-30167 Hannover, Germany⁸ Mathematical Sciences and STAG Research Centre, University of Southampton, Southampton SO17 1BJ, UK⁹ School of Physics, University of Melbourne, Parkville, Victoria 3010, Australia¹⁰ Anton Pannekoek Institute of Astronomy and GRAPPA, Science Park 904, University of Amsterdam, 1098XH Amsterdam, The Netherlands¹¹ School of Astronomy & Space Science, University of the Chinese Academy of Sciences, Beijing 100012, People's Republic of China¹² Max Planck Institute for Astrophysics, Karl-Schwarzschild-Str. 1, D-85748 Garching, Germany¹³ DARK, Niels Bohr Institute, University of Copenhagen, Jagtvej 128, DK-2200 Copenhagen, Denmark¹⁴ Niels Bohr International Academy, The Niels Bohr Institute, Blegdamsvej 17, DK-2100 Copenhagen, Denmark¹⁵ Department of Astronomy, University of Washington, Seattle, WA 98195, USA

Received 2021 October 1; revised 2021 November 24; accepted 2021 December 7; published 2022 February 2

Abstract

Compact Object Mergers: Population Astrophysics and Statistics (COMPAS; <https://compas.science>) is a public rapid binary population synthesis code. COMPAS generates populations of isolated stellar binaries under a set of parameterized assumptions in order to allow comparisons against observational data sets, such as those coming from gravitational-wave observations of merging compact remnants. It includes a number of tools for population processing in addition to the core binary evolution components. COMPAS is publicly available via the GitHub repository <https://github.com/TeamCOMPAS/COMPAS/>, and is designed to allow for flexible modifications as evolutionary models improve. This paper describes the methodology and implementation of COMPAS. It is a living document that will be updated as new features are added to COMPAS; the current document describes COMPAS v02.21.00.

Unified Astronomy Thesaurus concepts: [Stellar populations \(1622\)](#); [Binary stars \(154\)](#); [Neutron stars \(1108\)](#); [Black holes \(162\)](#)

Software reviewed by the [Journal of Open Source Software JOSS](#)

1. Introduction

The majority of massive stars are born in a stellar binary- or multiple-star system with other stellar companions (e.g., Chini et al. 2012; Sana et al. 2012, 2014; Kobulnicky et al. 2014; Almeida et al. 2017; Moe & Di Stefano 2017). The subsequent evolution of massive stellar binaries plays a critical role in many fields of astronomy. Massive binaries are thought to play key roles in the reionization of the universe (e.g., Conroy & Kratter 2012; Ma et al. 2016b; Eldridge et al. 2017; Rosdahl et al. 2018; Götberg et al. 2019, 2020), nucleosynthesis (e.g., Dray & Tout 2003; Izzard et al. 2006; Woosley & Heger 2007; Langer 2012), and the diversity of observed supernovae (e.g., Podsiadlowski et al. 1992; Eldridge et al. 2013, 2018, 2019a;

Tauris et al. 2015; Moriya et al. 2017; Yoon et al. 2017, 2019; Zapartas et al. 2019, 2021). Some massive binaries will evolve into systems containing one or two compact objects, which can be observed as X-ray binaries (e.g., Remillard & McClintock 2006), double neutron stars (e.g., Tauris et al. 2017), short gamma-ray bursts (e.g., Woosley & Bloom 2006; Berger 2014), and gravitational-wave transients (e.g., Mandel & Farmer 2018; Abbott et al. 2019; Mandel & Broekgaarden 2021).

Many physical processes in the evolution of a binary system are uncertain. The uncertainties in stellar wind mass loss, mass transfer, common envelope physics, supernova remnant masses, and natal kicks, among others, can be constrained by comparing the observed populations listed above against theoretical predictions under a range of assumptions. The essence of binary population synthesis (BPS) simulations is to enable modeling of large populations by combining prescriptions for single-star evolution (SSE) and binary star evolution (BSE), modeling the evolution of stars from zero-age main sequence (ZAMS) until their final states.

In this paper we present the publicly available BPS suite Compact Object Mergers: Population Astrophysics and Statistics (COMPAS). The core of COMPAS is a BPS code that models

¹⁶ The public COMPAS code is a product of work by the entire COMPAS collaboration over many years; we therefore kindly request that, in recognition of this team effort, the paper is cited as “Team COMPAS: J. Riley et al.”



the evolution of a population of binary stars using a set of simplified prescriptions or recipes for stellar and binary evolution. By doing so, COMPAS can compute the full evolution of a typical binary system in around 10 ms on a modern laptop, and compute the evolution of a million binaries in a few CPU hours. The general approach is similar to other BPS codes including the Scenario Machine (Lipunov et al. 1996a, 1996b, 2009), IBIS (Tutukov & Yungelson 1996), SeBa (Portegies Zwart & Verbunt 1996; Portegies Zwart & Yungelson 1998; Nelemans et al. 2001; Toonen et al. 2012), BSE (Hurley et al. 2002), StarTrack (Belczynski et al. 2002, 2008, 2020b), binary_c (Izzard et al. 2004, 2006, 2009), MOBSE (Giacobbo & Mapelli 2018; Giacobbo et al. 2018), and COSMIC (Breivik et al. 2020).

In addition to the core BPS code, COMPAS also provides several other publicly available tools, including rapid single stellar evolution, postprocessing tools to study the evolution of populations over cosmic time (Neijssel et al. 2019), post-processing scripts to model the detectability of double compact objects, or DCOs [comprising double neutron stars (DNS), binary black holes (BBH), and black hole–neutron star (BH–NS) mergers] by ground-based gravitational-wave observatories (e.g., Barrett et al. 2018), a statistical sampling framework to optimize the computational cost of BPS (Broekgaarden et al. 2019), and models for specific evolutionary phases such as X-ray binaries and pulsars (e.g., Chattopadhyay et al. 2020; Vinciguerra et al. 2020).

COMPAS was developed with a primary focus on the study of compact object mergers that serve as sources of gravitational waves. It has been used extensively to investigate the properties of compact binaries containing neutron stars and black holes. Stevenson et al. (2017) studied the formation history of the first three BBHs detected via gravitational waves. Barrett et al. (2018) explored how future gravitational-wave observations will allow us to determine the physics of massive binary evolution. Stevenson et al. (2019) included the impact of (pulsational) pair-instability supernovae. Neijssel et al. (2019) investigated the consequences of uncertain metallicity-specific star formation history on the rate and properties of DCO mergers. Lau et al. (2020) predicted the number of DNSs detectable with LISA and the inference these observations will enable. Bavera et al. (2020) used COMPAS to predict the spin distribution of merging BBHs. van Son et al. (2020) investigated the robustness of the predicted pair-instability mass gap to uncertainties in the accretion efficiency for black holes. Riley et al. (2021) studied chemically homogeneous evolution as a pathway to BBH formation. Mandel et al. (2021) considered the consequences of an alternative, stochastic recipe for compact remnant masses. Vigna-Gómez et al. (2021) explored sequential BBH mergers during triple evolution. Broekgaarden et al. (2021a) and Broekgaarden & Berger (2021) focused on the formation of black hole–neutron star binaries. van Son et al. (2021) investigated the relative contributions of dynamically stable and unstable mass transfer to BBH mergers over cosmic history. Broekgaarden et al. (2021b) investigated the relative impact from uncertain metallicity-specific star formation history to that from uncertain stellar evolution on the rate and properties of DCO mergers.

A number of other consequences of massive binary evolution have been explored with COMPAS. Vigna-Gómez et al. (2018) used observations of Galactic DNSs to constrain evolutionary physics. Chattopadhyay et al. (2020) used the same population to constrain birth distributions of pulsar spin periods and magnetic

field strengths, as well as magnetic field decay scales. Schröder et al. (2020) investigated optical counterparts to common envelope (CE) events which fail to eject the envelope and result in a merger. Howitt et al. (2020) explored luminous red novae: red optical transients associated with CE events. Vigna-Gómez et al. (2020) cataloged the CE events en route to DNS formation. Mandel & Müller (2020) took advantage of COMPAS SSE modules in formulating a stochastic compact remnant mass prescription and momentum-conserving natal kick prescription. Vinciguerra et al. (2020) studied the population of Be X-ray binaries to establish constraints for mass accretion efficiency. Chattopadhyay et al. (2021) explored the prospects for observing neutron star–black hole binaries in future radio pulsar surveys. Miller-Jones et al. (2021) and Neijssel et al. (2021) constrained the massive stellar wind mass loss with observations of the black hole (BH) high-mass X-ray binary Cygnus X-1. Willcox et al. (2021) compared COMPAS models to observed pulsar velocities in order to study neutron star natal kicks.

COMPAS has also played an important role in developing more efficient sampling, inference, and model emulation techniques. Barrett et al. (2017) attempted to generate computationally efficient surrogate models of binary population synthesis through Gaussian process emulation. Taylor & Gerosa (2018) used COMPAS public data as an example in their hierarchical inference study. Broekgaarden et al. (2019) applied importance sampling to enable computationally efficient DCO simulations. Lin et al. (2021) developed new tools for classification and emulation based on (local) Gaussian process models and the COMPAS suite.

In this paper we introduce the COMPAS code and discuss its methodology and implementation. The paper is organized as follows. Section 2 presents the main features of COMPAS. Section 3 discusses the implementation of single stellar evolution in COMPAS. Section 4 discusses binary stellar evolution prescriptions. In Section 5 we describe how COMPAS can be used to model populations of binaries. Section 6 describes the postprocessing tools available within COMPAS. Section 7 illustrates a few applications of COMPAS. We conclude in Section 8.

2. COMPAS

2.1. Overview

COMPAS¹⁷ is an open-source integrated suite of software tools combining a robust, rapid, and flexible population synthesis application for both single-star evolution and binary star evolution, with tools for deployment on a range of platforms, including high-performance computing platforms, and a set of Python postprocessing analysis and plotting scripts.

The heart of the COMPAS suite is the SSE and BSE simulation code, developed in the C++ programming language. C++ is a cross platform, object-oriented programming (OOP) language that gives a clear structure to programs and allows code to be easily understood and maintained—it is one of the world’s most popular programming languages, and has an established history of being used to create high-performance applications. The COMPAS C++ code is a modular, object-oriented code, designed to be easily understood and extended.

Results produced with COMPAS are publicly available.¹⁸

¹⁷ compas.science. Code available at <https://github.com/TeamCOMPAS/COMPAS>.

¹⁸ <https://zenodo.org/communities/compas/>

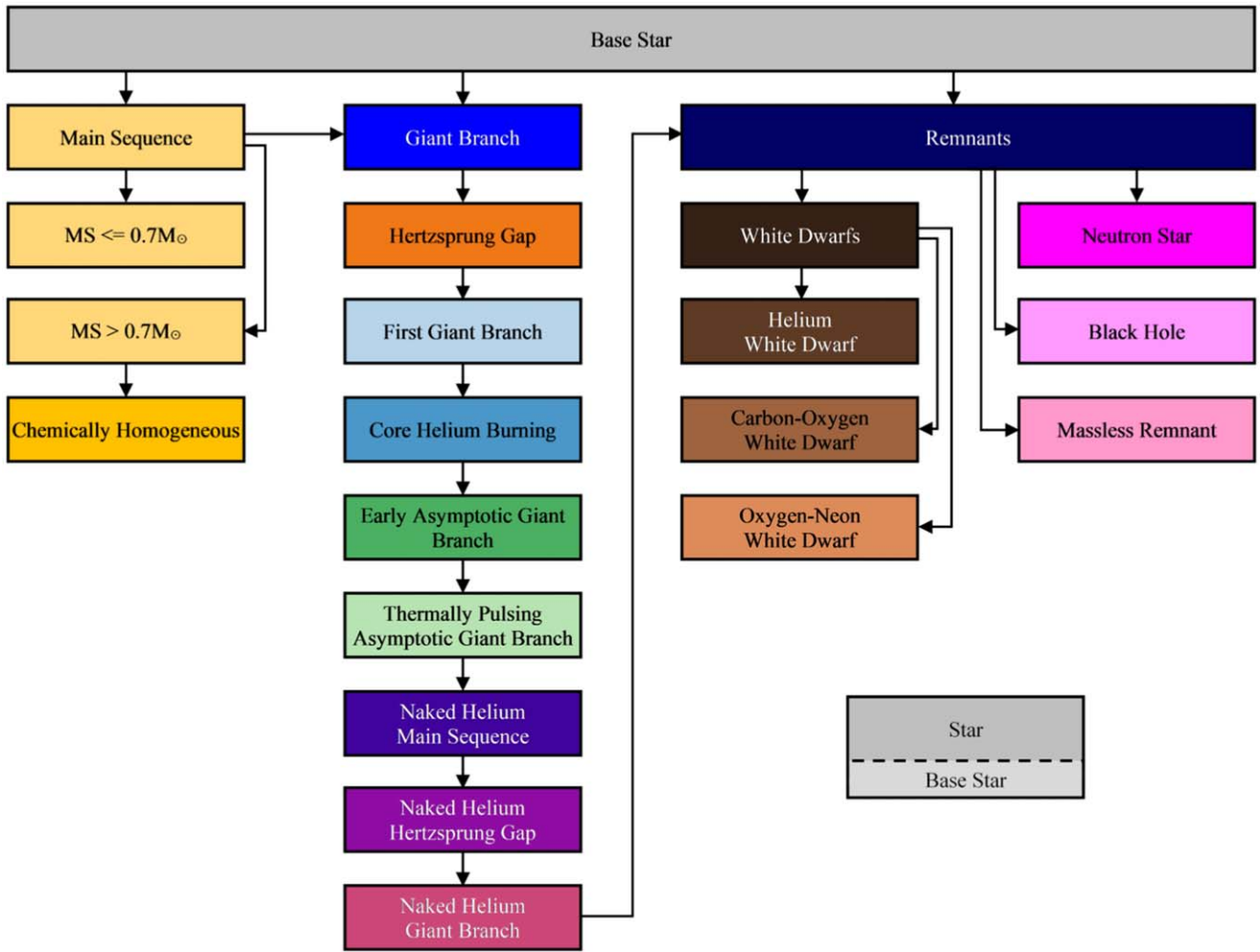


Figure 1. SSE class and container diagram (arrows indicate inheritance).

2.2. Mode: Single Star versus Binary Star

COMPAS operates in either one of two selectable modes: SSE or BSE. As the names suggest, in SSE mode COMPAS evolves single stars, and in BSE mode COMPAS evolves binary stars.

The SSE algorithm covers all evolution phases from the ZAMS up to and including the remnant stages. The allowed range of ZAMS masses, $M \in [0.1, 150] M_{\odot}$, extends the range of Hurley et al. (2000) models by extrapolation; the allowed range of metallicities $Z \in [10^{-4}, 0.03]$ follows these models (see Section 3 for a full description).

In BSE mode, the SSE code provides the stellar attributes (e.g., luminosity, radius, temperature, etc.) for each of the component stars as they evolve. COMPAS evolves binary stars until a DCO is formed, the component stars merge, or, optionally, the binary is disrupted.

In either mode (SSE or BSE), users can specify a maximum evolution time and/or maximum number of evolutionary steps, after which evolution is halted.

2.3. Architecture

The SSE and BSE simulation code at the heart of COMPAS is written in C++ using OOP concepts. The architecture is based on stellar type, with each stellar type being described by a separate C++ class. Figure 1 shows the SSE class and

container diagram, where the arrows indicate inheritance (the OOP mechanism used to base one class upon another: the inheriting class inherits the implementation of the inherited class). The COMPAS C++ code is implemented using multiple inheritance, and all stellar classes also inherit directly from the *BaseStar* class (arrows not shown in Figure 1 for clarity). Each of the stellar classes encapsulates data structures and algorithms specific to the evolutionary phase corresponding to the class.¹⁹

The *Star* class shown in Figure 1 is a container class for the stellar classes. An instance of the *Star* class is a single star being evolved by COMPAS, and contains an object that is created as a *BaseStar* object, and evolves, over time, through various SSE classes shown in Figure 1.

Figure 2 shows the BSE class and container diagram. The main class for binary star evolution is the *BinaryStar* class. The *BinaryStar* class is a wrapper, containing a *BaseBinaryStar* class object, and abstracts away the details of the binary star and the evolution. The *BaseBinaryStar* class is a container class for the objects that represent the component stars of a binary system. An instance of the *BaseBinaryStar* class is a binary system being evolved by COMPAS, and contains a *BinaryConstituentStar* class object for each of the component stars

¹⁹ The class names shown in Figure 1 do not match the class names used in the COMPAS C++ code, which are abbreviated into single words or acronyms.

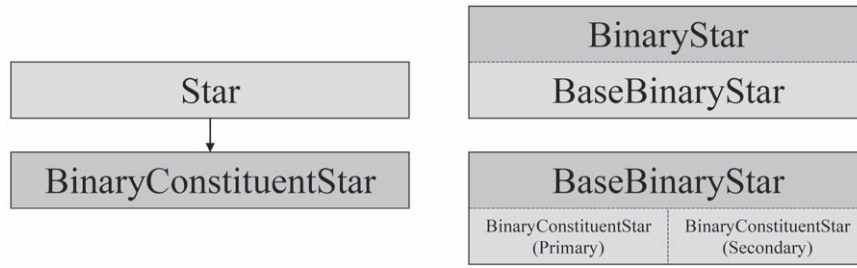


Figure 2. BSE class and container diagram.

(i.e., the primary and secondary stars), as well as data structures and algorithms specific to the evolution of a binary system. The *BinaryConstituentStar* class inherits from the SSE *Star* class, so objects instantiated from the *BinaryConstituentStar* class inherit the characteristics of the SSE *Star* class, particularly the stellar evolution model. The *BinaryConstituentStar* class defines additional data structures and algorithms (to the data structures and algorithms provided by the SSE classes) required to support the evolution of a binary system component star.

2.4. Evolutionary Models

2.4.1. SSE Model

The SSE model implemented in COMPAS (see Section 3 for more details) follows Hurley et al. (2000), using their analytical fits to the models of Pols et al. (1998). After the creation of the star according to the initial conditions (specified or sampled), the evolution of a single star proceeds by integrating the attributes of the star over its lifetime, and stops when the star evolves to a remnant, or the maximum time, or maximum number of time steps is reached.

Figure 3 shows a high-level overview of the code flow for SSE.

2.4.2. BSE Model

The binary evolution model implemented in COMPAS is broadly similar to the BSE population synthesis application (Hurley et al. 2002), and other population synthesis applications derived from it, such as *binary_c* (Izzard et al. 2004, 2006, 2009; De Minkde Mink et al. 2013) and *StarTrack* (Belczynski et al. 2002, 2008).

After the creation of the binary system according to the initial conditions (specified or sampled), the evolution of a binary system proceeds by integrating the attributes of the system over its lifetime and stops if the component stars merge, when the system forms a DCO, is disrupted, or the maximum time or maximum number of time steps is reached.

Figure 4 shows a high-level overview of the code flow for BSE.

2.5. Time Stepping

The initial estimate of the time step used in SSE follows Hurley et al. (2000), where the time step varies depending upon the evolutionary phase of the star (see Section 3 for a full list of the stellar types). COMPAS then checks whether the time step produces excessive change, defined as either

1. mass loss greater than 1%, or
2. radial change greater than 10%

over the time step, and limits the time step accordingly.

For nuclear timescale evolution, we limit the time step to a minimum of 100 yr, and we impose an overall minimum time

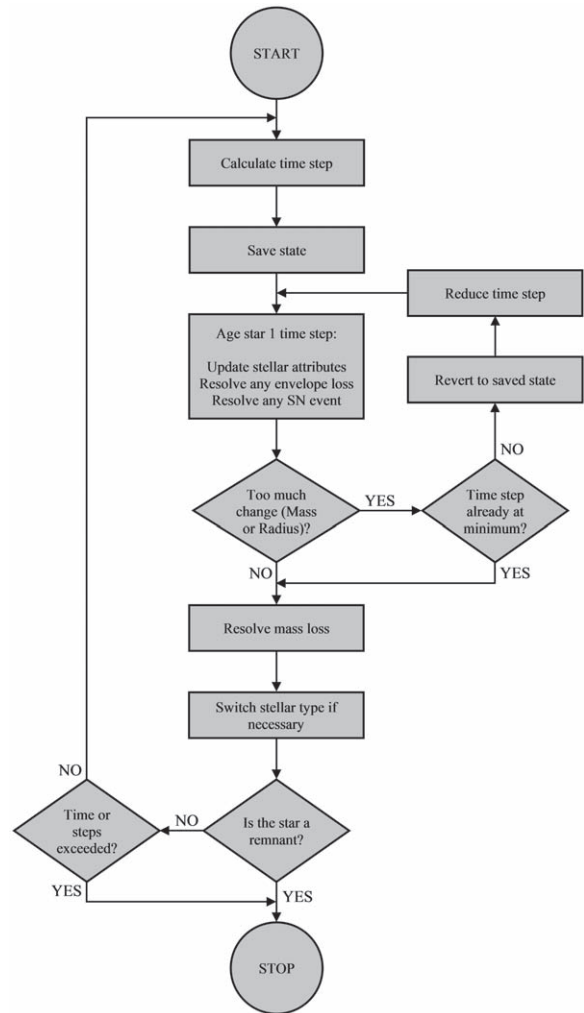


Figure 3. High-level SSE evolution.

step of 100 s, including for dynamical timescale evolution (see Section 3.3).

For the BSE time step, COMPAS uses the minimum of the binary constituent stars’ SSE time steps: this allows the constituent stars to evolve using time steps that do not produce excessive change. Changes in binary properties are not separately considered when calculating the time step since large changes in binary properties would be accompanied by similarly large changes in constituent star properties.

COMPAS provides a mechanism for the user to scale the calculated time step by a positive scaling factor. Scaling is performed prior to limiting of the time step.

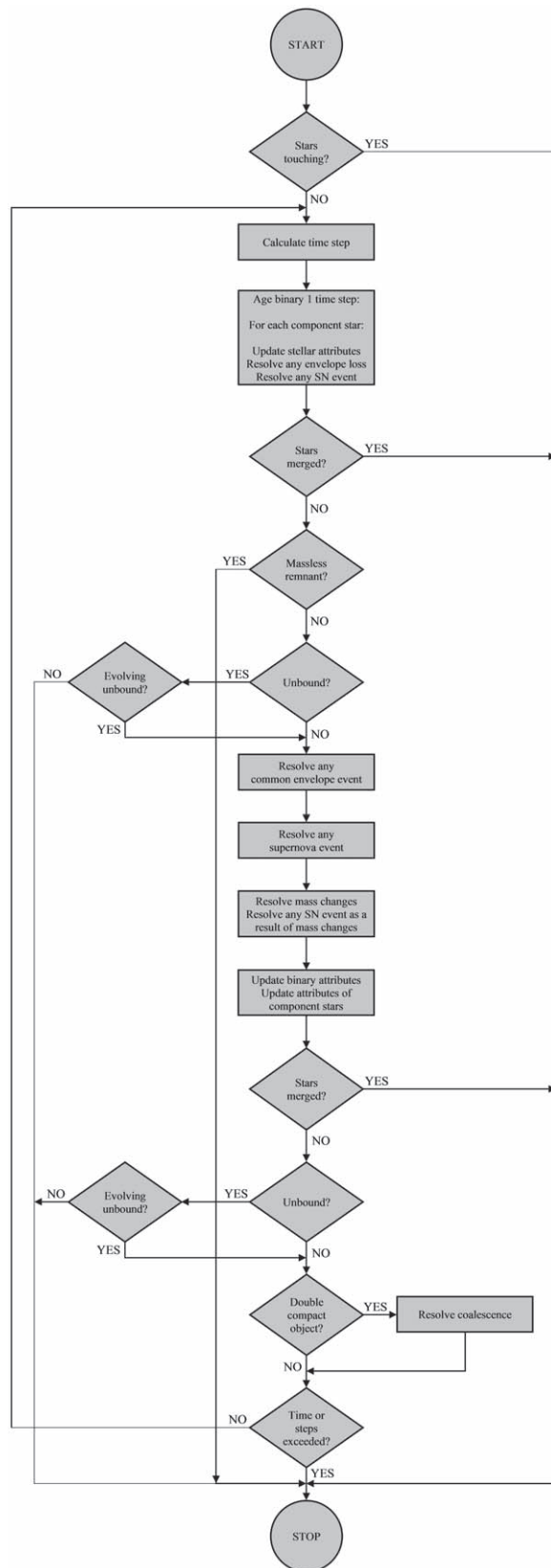


Figure 4. High-level BSE evolution.

2.6. Input and Configuration

COMPAS provides wide-ranging functionality and affords users much flexibility in determining how the synthesis and evolution of stars (single or binary) is conducted. Users

configure COMPAS’S functionality and provide initial conditions via the use of program options and input grid files. The full list and description of program options and grid files can be found in the COMPAS online documentation.²⁰

2.7. Default Model

Investigating massive star and binary evolution requires modeling many complicated astrophysical processes. In BPS codes, this is often done through the use of simple analytic prescriptions, which are calibrated either to theoretical predictions or to results from observations (see Sections 3 and 4 for more details in the context of SSE and BSE). In this paper, we refer to our default set of modeling assumptions, including which prescriptions are used, as our *Default* (or “default”) model. This model is summarized in Table 1. This model has been calibrated to match a range of observations (see Section 1 for a brief overview). There are, however, large uncertainties in the prescriptions used. COMPAS is flexible, and in many cases, we provide additional options to allow users to easily vary their choices from our defaults.

2.7.1. Program Options

COMPAS provides a rich set of configuration parameters via program options, allowing users to vary many parameters that define the initial attributes and/or affect the evolution of single and binary stars being evolved. Furthermore, COMPAS allows some parameters to be specified as ranges or sets of values via the program options, allowing users to specify a grid of parameter values on the command line. Combining command line program options, particularly ranges and sets, with a grid file allows users great flexibility in specifying more complex combinations of parameter values.

2.7.2. Grid Files

A grid file allows users to specify, in plain text, initial values and physics assumptions for multiple systems for both SSE and BSE. Each line of a grid file is used by COMPAS to set the initial values of an individual single star (SSE) or an individual binary system (BSE), and the physics assumptions to be used to evolve the star or system.

2.8. Output

COMPAS provides real-time status information during the evolution of systems. Detailed and summary information about the star or system being evolved is written to log files as the evolution proceeds.

A number of COMPAS log files may be produced depending upon the simulation type (SSE or BSE) and user specifications. These log files record, for each star or system being evolved:

1. summary information at the completion of evolution,
2. detailed information at each time step,
3. detailed information at the time of each stellar type switch,
4. summary information for all supernovae (SNe) events,
5. summary information for all CE events during BSE,
6. detailed information for all Roche-lobe overflow (RLOF) events during BSE,
7. summary information for all DCOs formed during BSE, and

²⁰ <https://compas.science/docs/>

Table 1
Initial Values and Default Settings for Binary Population Synthesis Simulation with COMPAS

Description and Name	Value/Range	Note/Setting
Initial conditions		
Initial mass $M_{1,i}$	[5, 150] M_{\odot}	Kroupa (2001) IMF $\propto M_{1,i}^{-\alpha_{\text{IMF}}}$ with $\alpha_{\text{IMF}} = 2.3$ for stars in this mass range
Initial mass ratio $q_i = M_{2,i}/M_{1,i}$	[0.01, 1]	We assume a flat mass ratio distribution $p(q_i) \propto 1$ with $M_{2,i} \geq 0.1 M_{\odot}$
Initial semimajor axis a_i	[0.01, 1000] au	Distributed flat-in-log $p(a_i) \propto 1/a_i$
Initial metallicity Z_i	[0.0001, 0.03]	Distributed flat-in-log $p(Z_i) \propto 1/Z_i$
Initial orbital eccentricity e_i	0	All binaries are assumed to be circular at birth
Fiducial parameter settings		
Chemically homogeneous evolution	Enabled	Following Riley et al. (2021), “pessimistic” version checking for threshold throughout evolution (Section 3.4).
Stellar winds for hydrogen-rich stars	Belczynski et al. (2010)	Based on Vink et al. (2000, 2001), including LBV wind mass loss with $f_{\text{LBV}} = 1.5$.
Stellar winds for hydrogen-poor helium stars	Belczynski et al. (2010)	Based on Hamann & Koesterke (1998) and Vink & de Koter (2005).
Mass-transfer stability criteria	ζ -prescription	Based on Vigna-Gómez et al. (2018) and references therein
Mass-transfer accretion rate	Thermal timescale Eddington-limited	Limited by thermal timescale for stars Vigna-Gómez et al. (2018), Vinciguerra et al. (2020) Accretion rate is Eddington-limited for compact objects
Nonconservative mass loss	Isotropic re-emission	Mashevitch & Yungelson (1975), Bhattacharya & van den Heuvel (1991) Soberman et al. (1997), Tauris & van den Heuvel (2006)
Case BB mass-transfer stability	Always stable	Based on Tauris et al. (2015, 2017), Vigna-Gómez et al. (2018) (Section 4.2)
Circularization at the onset of RLOF	On	Instantly circularized to periaapsis (Section 4.2)
CE prescription	$\alpha - \lambda$	Based on Webbink (1984), de Kool (1990)
CE efficiency α -parameter	1.0	(Section 4.2.4)
CE λ -parameter	λ_{Nanjing}	Based on Xu & Li (2010a, 2010b) and Dominik et al. (2012)
Hertzsprung gap (HG) donor in CE	Pessimistic	Defined in Dominik et al. (2012): HG donors do not survive a CE phase
SN natal-kick magnitude for white dwarfs	0	We assume WDs do not receive natal kicks (Section 3.7.1)
SN natal-kick magnitude v_k for NS	$[0, \infty)$ km s ⁻¹	Drawn from Maxwellian distribution with standard deviation $\sigma_{\text{rms}}^{\text{1D}}$
SN natal-kick magnitude for BH	$[0, \infty)$ km s ⁻¹	Reduced relative to NS kicks by the fallback fraction (Fryer et al. 2012), see Section 3.9
SN natal-kick polar angle θ_k	$[0, \pi]$	$p(\theta_k) = \sin(\theta_k)/2$
SN natal-kick azimuthal angle ϕ_k	$[0, 2\pi]$	Uniform $p(\phi) = 1/(2\pi)$
SN mean anomaly of the orbit	$[0, 2\pi]$	Uniformly distributed
Core-collapse SN remnant mass prescription	Delayed	From Fryer et al. (2012), which has no lower BH mass gap
USSN remnant mass prescription	Delayed	From Fryer et al. (2012)
ECSN remnant mass prescription	$m_f = 1.26 M_{\odot}$	Based on Equation (8) in Timmes et al. (1996)
Core-collapse SN velocity dispersion $\sigma_{\text{rms}}^{\text{1D}}$	265 km s ⁻¹	1D rms value based on Hobbs et al. (2005)
USSN and ECSN velocity dispersion $\sigma_{\text{rms}}^{\text{1D}}$	30 km s ⁻¹	1D rms value based on e.g., Pfahl et al. (2002a), Podsiadlowski et al. (2004)
PISN/PPISN remnant mass prescription	Marchant et al. (2019)	As implemented in Stevenson et al. (2019)
Maximum NS mass	$\text{max}_{\text{NS}} = 2.5 M_{\odot}$	Mass division between NS and BH (Section 3.7.2)
Tides and rotation		No tides and/or rotation except chemically homogeneous evolution
Simulation settings		
Binary fraction	$f_{\text{bin}} = 1$	Corrected factor to be consistent with, e.g., Sana (2017)
Solar metallicity Z_{\odot}	$Z_{\odot} = 0.0142$	Based on Asplund et al. (2009)

Note. COMPAS users who wish to provide a similar table accompanying their publication can find a template at <https://github.com/FloorBroekgaarden/templateForTableBPSsettings>.

8. detailed pulsar evolution information.

COMPAS log files are created and written as hierarchical data format, version 5 (HDF5) files,²¹ comma separated values (CSV) files, tab separated values (TSV) files, or plain text files, as specified by the user.

The COMPAS software suite includes a Python postprocessing script to combine all COMPAS output HDF5, CSV, or TSV files into a single HDF5 file, which is especially useful if a single large experiment is spread over several virtual machines.

3. Single Stellar Evolution

As stars evolve, they experience nuclear fusion while balancing gravity with pressure and radiating away excess energy.

²¹ <https://www.hdfgroup.org/>

Consequently, their composition, radius, temperature, and luminosity all change, they may lose mass in stellar winds, and sufficiently massive stars may explode in SNe at the end of their lives.

COMPAS currently relies on rapid algorithms that provide estimates for how various fundamental stellar properties, such as their radii and luminosities, change as a star evolves through different evolutionary phases. The algorithms that capture how stars evolve—the SSE library—are at the core of the COMPAS code. These routines govern the evolution of single stars, as the name suggests, but they are also used to capture how a star evolves under the external influence of a binary companion.

In this section we begin by giving an overview of the evolutionary algorithms implemented in COMPAS that govern the evolution of the main properties of stars (Section 3.1). We then discuss some of the key evolutionary stages that stars evolve through (Section 3.2), and highlight several important evolutionary timescales in stellar evolution (Section 3.3). We proceed to describe the effects of rapid rotation that are included in COMPAS (Section 3.4), and describe the prescriptions available in COMPAS for incorporating mass loss in stellar winds (Section 3.5). We end this section by discussing the properties of stellar remnants: white dwarfs (WDs), neutron stars (NSs), and BHs.

3.1. Evolutionary Algorithms

COMPAS computes the properties of a star (such as luminosity, radius, or core mass) as functions of a star’s mass, metallicity, and age using analytic formulae, fit to detailed stellar models. The ZAMS radius R_{ZAMS} and luminosity L_{ZAMS} are calculated as functions of mass and metallicity using the analytic formulae from Tout et al. (1996). During the evolution we use the formulae from Hurley et al. (2000), developed to match the detailed stellar models of Pols et al. (1998; see also Eggleton et al. 1989 and Tout et al. 1997 for the basis of this approach).

The Pols et al. (1998) stellar models are for nonrotating stars and span ZAMS masses between 0.1–50 M_{\odot} . The original models do not include any mass loss. We incorporate mass loss following Hurley et al. (2000) as described in Section 3.5. Since the Hurley et al. (2000) formulae are polynomials in M_{ZAMS} , they can easily be extrapolated to higher masses by evaluating them outside of this range. We find that the fits extrapolate smoothly to at least 150 M_{\odot} . We note that this approach is not ideal, but significantly improving upon this is far from trivial. The evolution of high-mass stars is still very uncertain (Maeder & Meynet 2000; Langer 2012; Agrawal et al. 2020; Bowman 2020; Belczynski et al. 2021). This is particularly true for the later, faster evolutionary phases, where observations are scarce, and for internal properties such as core masses, which we cannot probe directly. Although grids of detailed models exist, they vary widely in their predictions. Given the limitations in the accuracy of massive star models and the absence of robust rapid prescriptions that clearly provide a significant improvement, we opt for simply extrapolating the fits in the present version of COMPAS.

The models are applicable for metallicities between $Z = 10^{-4}$ and $Z = 0.03$. We *do not* extrapolate in metallicity, as we find that some of the fitting formulae are not well behaved outside of this range. We discuss the implications for population studies in Section 6.4.

3.2. Evolutionary Stages

To introduce some of the evolutionary stages captured by the SSE formulae, we briefly summarize the main evolutionary stages of single stars. Our extremely brief sketch of stellar evolution generally follows the characteristic behavior of massive stars, and should not be taken as fully general.

We follow the lives of stars from the ZAMS (we do not include pre-main-sequence evolution in COMPAS). Stars spend most of their lives on the main sequence, fusing hydrogen in their cores. Following Hurley et al. (2000), we distinguish between low-mass ($M_{\text{ZAMS}} \leq 0.7 M_{\odot}$) main-sequence stars (stellar type 0) which are expected to be fully convective, and more massive main-sequence stars ($M_{\text{ZAMS}} > 0.7 M_{\odot}$, stellar type 1). During main-sequence evolution, most stars increase their luminosity and decrease their effective temperature T_{eff} . Following the main sequence, sufficiently massive stars experience a rapid thermal timescale (see Section 3.3) phase of expansion, evolving to lower effective temperatures at near constant luminosity. This phase of evolution is sometimes known as the Hertzsprung gap (HG), as the short timescale leads to a paucity of stars observed in this phase. Stars then begin a longer-lived phase of core helium burning (CHeB), evolving onto and up the giant branch. We note that at low metallicity, massive stars may not reach the giant branch before beginning CHeB. Helium-shell-burning stars evolve along the asymptotic giant branch (AGB). We choose to use the name early asymptotic giant branch (EAGB) for H-rich massive stars with a C/O core, in addition to its usual meaning. Stars that lose their outer hydrogen envelopes, either through stellar winds or binary mass transfer, become helium main-sequence (HeMS) stars, which then evolve analogously to hydrogen-rich stars through to the helium giant branch (HeGB). Finally, most stars end their lives as a stellar remnant, either a WD, NS, or BH depending on their initial mass, while some stars leave behind no remnant.

We show the evolution of single stars of particular masses in the mass range 0.5–150 M_{\odot} at solar ($Z = 0.0142$, Asplund et al. 2009) and low ($Z = 0.001$) metallicity in the Hertzsprung–Russell diagram according to COMPAS in Figure 5, with the different evolutionary phases identified for each track.

A complete list of stellar phases is given in Table 2, following Hurley et al. (2000). See Figure 1 for a schematic of the corresponding classes in the COMPAS code.

Figure 6 shows the maximum radial extent of a star during each evolutionary phase for a star with ZAMS mass between 0.5–150 M_{\odot} at solar ($Z = 0.0142$) and low ($Z = 0.001$) metallicity. Phases during which a star expands are the phases when binary interactions are most likely to occur. We discuss binary interactions further in Section 4.

3.3. Evolutionary Timescales

Three key timescales in single and binary stellar evolution—dynamical, thermal, and nuclear—often create a very convenient timescale hierarchy. The separation of timescales allows many approximations to be made.

The shortest timescale is almost always the dynamical (or freefall) timescale, defined as

$$\tau_{\text{dyn}} = \sqrt{\frac{R^3}{GM}} \approx 1600 \text{ s} \left(\frac{R}{R_{\odot}} \right)^{3/2} \left(\frac{M}{M_{\odot}} \right)^{-1/2}, \quad (1)$$

where R is the radius of a star and M is its mass. The dynamical timescale is used as the minimum timescale in COMPAS (with a minimum cutoff of 100 s).

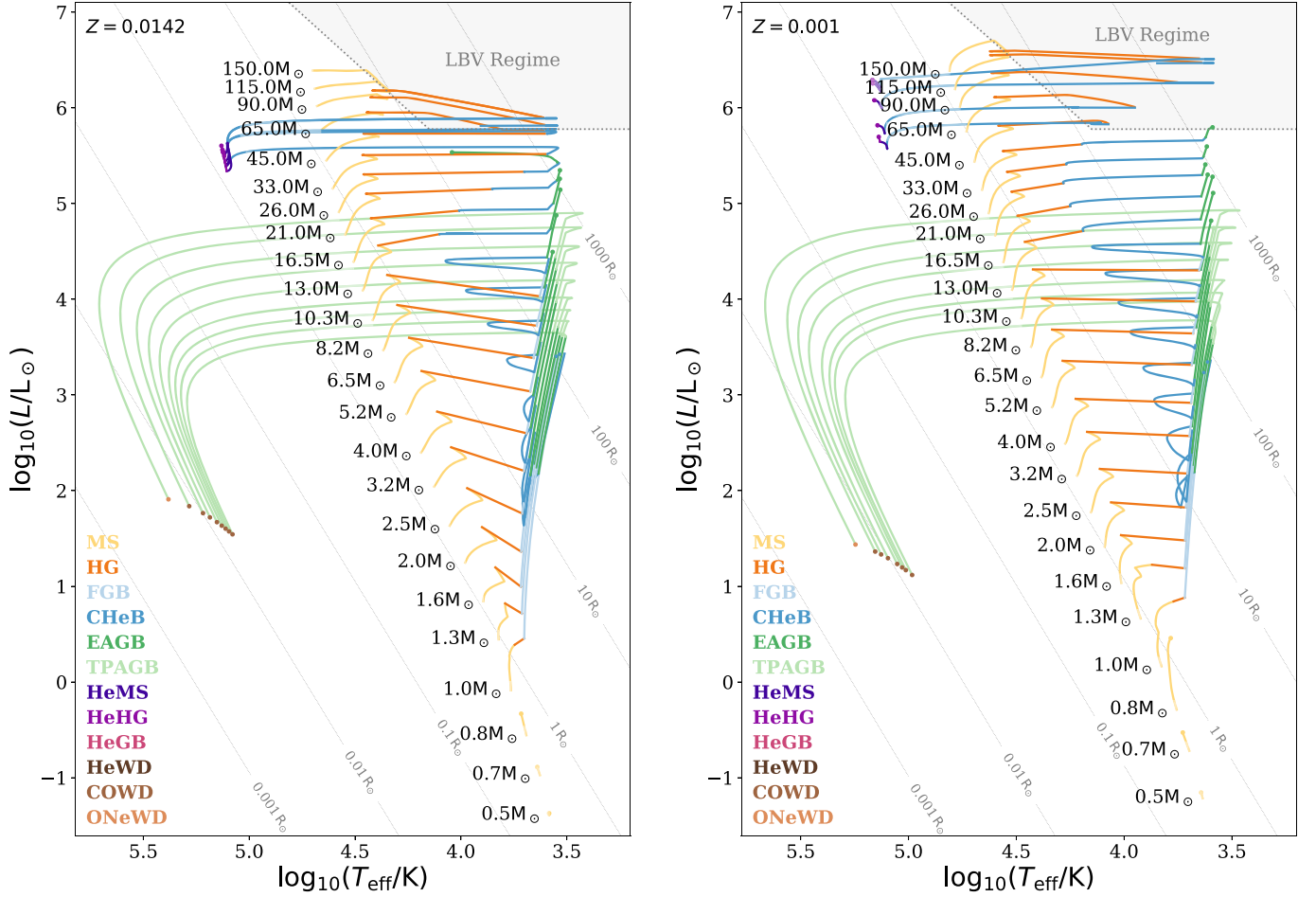


Figure 5. Evolutionary tracks in the Hertzsprung–Russell diagrams for single stars with ZAMS masses between 0.5–150 M_{\odot} at solar ($Z = 0.0142$) and low ($Z = 0.001$) metallicity using COMPAS default settings, limited to a maximum evolution time of 14 Gyr. The shaded region (bounded by the Humphreys–Davidson limit and a minimum luminosity) illustrates the regime in which luminous blue-variable (LBV) mass loss dominates. Diagonal contours show lines of constant radii.

The Kelvin–Helmholtz (or thermal) timescale is the time required for a star’s internal energy E_{int} to be radiated at its current luminosity L , and is given by $\tau_{\text{KH}} = E_{\text{int}}/L$. We estimate this as

$$\tau_{\text{KH}} \approx 3.0 \times 10^7 \text{ yr} \left(\frac{M}{M_{\odot}} \right) \left(\frac{M_{\text{s/env}}}{M_{\odot}} \right) \left(\frac{R}{R_{\odot}} \right)^{-1} \left(\frac{L}{L_{\odot}} \right)^{-1}, \quad (2)$$

where L is the luminosity of the star and $M_{\text{s/env}}$ is either the total mass of the star M for stellar types without a clearly defined envelope, or the mass of the envelope M_{env} for stars with a clearly defined envelope (see Hurley et al. 2002, for more details). This is used, e.g., when calculating thermal timescale mass transfer (see Section 4.2.3).

The nuclear timescale is relevant when nuclear fusion is setting the timescale at which the star evolves. This applies, e.g., to main-sequence stars that burn hydrogen in their centers, and stars that are undergoing central helium burning. The nuclear timescale is approximately

$$\tau_{\text{nuc}} \approx \phi f_{\text{nuc}} \frac{Mc^2}{L} \approx 10^{10} \text{ yr} \left(\frac{M}{M_{\odot}} \right) \left(\frac{L}{L_{\odot}} \right)^{-1}, \quad (3)$$

where c is the speed of light, ϕ is the efficiency which the rest mass of the relevant reacting nuclei is converted into energy

(for hydrogen, $\phi = 0.007$), and f_{nuc} is the fraction of the stellar mass that can serve as nuclear fuel. We do not use this timescale in any calculations; it is provided here, and optionally in COMPAS outputs, for reference only. Instead, we use the fitting formulae for stellar lifetimes in Hurley et al. (2000). The main-sequence lifetimes given by these fits are shown in Figure 7. At masses of $\gtrsim 50 M_{\odot}$ the Hurley et al. (2000) formulae, which extrapolate the Pols et al. (1998) model grid in this mass range, overestimate the stellar lifetimes by approximately 30% compared to the detailed stellar models considered in Agrawal et al. (2020).

3.4. Rotation

Most stars rotate sufficiently slowly (e.g., Dufton et al. 2013; Ramírez-Agudelo et al. 2013) for the impact of rotation to be modest. Rotation is expected to enhance mass-loss rates (e.g., Chiosi & Maeder 1986; Friend & Abbott 1986; see also Section 3.5), slightly increase main-sequence luminosities and lifetimes (e.g., Talon et al. 1997; Maeder & Meynet 2000), and lead to increased core masses (e.g., Maeder 1987; Langer 1992; Heger et al. 2000).

However, very rapid rotation, especially coupled with significant tidal effects in very close binaries, can have a dramatic impact on the evolution of a star. Sufficiently rapid rotation can lead to

enhanced mixing within a star, which may lead to chemically homogeneous evolution (Maeder 1987), where a star can burn almost all of its hydrogen into helium.

The stellar tracks used in COMPAS are based on nonrotating stellar models (Pols et al. 1998). We do not account for the effects of mild rotation, but we do implement chemically homogeneous evolution (CHE) following the recipes of Riley et al. (2021). COMPAS implements a metallicity-dependent rotational frequency threshold to determine whether a star is evolving chemically homogeneously. If a star is rotating faster than the threshold given by Riley et al. (2021) at ZAMS, we consider it to be evolving chemically homogeneously. We neglect the very limited radial evolution of a CHE star and fix its main-sequence radius equal to the ZAMS radius of a nonrotating star of the same mass and metallicity. The main-sequence evolution of a CHE star thus follows the Hurley et al. (2000) model of main-sequence stars, albeit with a fixed radius. COMPAS can be configured by the user to check, or not, the rotational frequency of the star against the CHE threshold at every time step on the main sequence. In the default model, the rotational frequency check is enabled, and if the rotational frequency drops below the threshold value for CHE (e.g., due to the orbit of the binary widening as a consequence of mass loss through winds), the star is thereafter evolved as a regular main-sequence star (i.e., it immediately jumps to the track of a regular main-sequence star of the same mass). If the rotational frequency check is disabled by the user, the star evolves chemically homogeneously through its main-sequence lifetime once it satisfies the CHE threshold at ZAMS. Finally, we assume that if a star evolves chemically homogeneously through the main sequence, it contracts directly into a naked helium star at the end of the main sequence, retaining its full mass at that point. Evolution then follows the Hurley et al. (2000) models of helium stars.

3.5. Wind Mass Loss (Single Star)

Stars lose mass through stellar winds. This impacts their evolution, and affects what remnants they form. Stars lose mass throughout their lives through several mechanisms. Hot stars lose mass through steady-state line-driven winds (Castor et al. 1975; Vink et al. 2001), while the mechanism through which cool stars like red supergiants (RSGs) lose mass is less well understood theoretically, leading to most mass-loss prescriptions for these stars being empirically derived (e.g., de Jager et al. 1988; Beasor & Davies 2018). In addition, stars close to the Humphreys–Davidson limit (Humphreys & Davidson 1994) are known to experience eruptive mass loss. For a review of mass loss from massive stars, see Smith (2014). Low-mass stars generally experience weaker stellar winds than their high-mass counterparts. However, they can experience strong wind mass loss during the later stages of their evolution on the AGB (see, e.g., Höfner & Olofsson 2018, for a recent review).

Wind mass-loss rates are highly uncertain, and can have a substantial impact on the evolution of a star (e.g., Renzo et al. 2017; Belczynski et al. 2020a). There is recent observational evidence that mass-loss rates may be overestimated for certain evolutionary phases (e.g., Smith 2014; Beasor & Davies 2018; Sander et al. 2020; Miller-Jones et al. 2021; Neijssel et al. 2021).

COMPAS currently includes two simple analytic prescriptions for wind mass loss based on a combination of theoretical simulations and observational measurements: the original wind

Table 2
Stellar Phases and Abbreviations Used in COMPAS

Stellar Phase	Abbreviation	Number
Main sequence, $M < 0.7 M_{\odot}$	MS	0
Main sequence, $M > 0.7 M_{\odot}$	MS	1
Hertzsprung gap	HG	2
First giant branch	FGB	3
Core helium burning	CHeB	4
Early asymptotic giant branch ^a	EAGB	5
Thermally pulsing asymptotic giant branch	TPAGB	6
Helium main sequence	HeMS	7
Helium Hertzsprung gap	HeHG	8
Helium giant branch	HeGB	9
Helium white dwarf	HeWD	10
Carbon–oxygen white dwarf	COWD	11
Oxygen–neon white dwarf	ONeWD	12
Neutron star	NS	13
Black hole	BH	14
Massless remnant	MR	15
Chemically homogeneously evolving	CHE	16
...	NONE ^b	19

Notes. Types 0–15 are from Hurley et al. (2000), while CHE stars (type 16) are an addition in COMPAS (Riley et al. 2021).

^a We apply the term EAGB to all H-rich stars with an inert C/O core that are primarily powered by He shell fusion, regardless of mass or location in the Hertzsprung–Russell diagram.

^b Stellar type 19 (NONE) can sometimes appear as a temporary placeholder in COMPAS outputs before the stellar type is set.

prescription from Hurley et al. (2000) and an updated prescription from Belczynski et al. (2010), which is our default.

3.5.1. Hurley Model

Hurley et al. (2000) define the total mass-loss rate as the dominant mass-loss rate during each stellar phase of the star (see Table 2), with a possible addition of LBV-like mass loss if the star is an luminous blue variables (LBV). This can be summarized as

$$\dot{M}_H = \begin{cases} \dot{M}_{\text{NJ}}, & \text{MS} \\ \max\{\dot{M}_{\text{NJ}}, \dot{M}_{\text{KR}}, \dot{M}_{\text{WR}}\} + \dot{M}_{\text{LBV}}, & \text{if HG-CHeB} \\ \max\{\dot{M}_{\text{NJ}}, \dot{M}_{\text{KR}}, \dot{M}_{\text{WR}}, \dot{M}_{\text{VW}}\}, & \text{AGB} \\ \max\{\dot{M}_{\text{NJ}}, \dot{M}_{\text{KR}}, \dot{M}_{\text{WR}}(\mu = 0)\}, & \text{HeMS-HeGB} \\ 0, & \text{otherwise,} \end{cases} \quad (4)$$

where \dot{M}_{NJ} , \dot{M}_{KR} , \dot{M}_{WR} , \dot{M}_{VW} , \dot{M}_{LBV} are defined as follows.

For stars across the whole Hertzsprung–Russell (HR) diagram, Hurley et al. (2000) apply

$$\begin{aligned} \dot{M}_{\text{NJ}} = & 9.6 \times 10^{-15} \max\left(0, \min\left(1, \frac{(L/L_{\odot}) - 4000}{500}\right)\right) \\ & \times \left(\frac{Z}{0.02}\right)^{1/2} \left(\frac{R}{R_{\odot}}\right)^{0.81} \\ & \times \left(\frac{L}{L_{\odot}}\right)^{1.24} \left(\frac{M}{M_{\odot}}\right)^{0.16} M_{\odot} \text{ yr}^{-1}, \end{aligned} \quad (5)$$

which is the mass-loss rate from Nieuwenhuijzen & de Jager (1990), modified by the metallicity scaling $Z^{1/2}$ (Kudritzki et al.

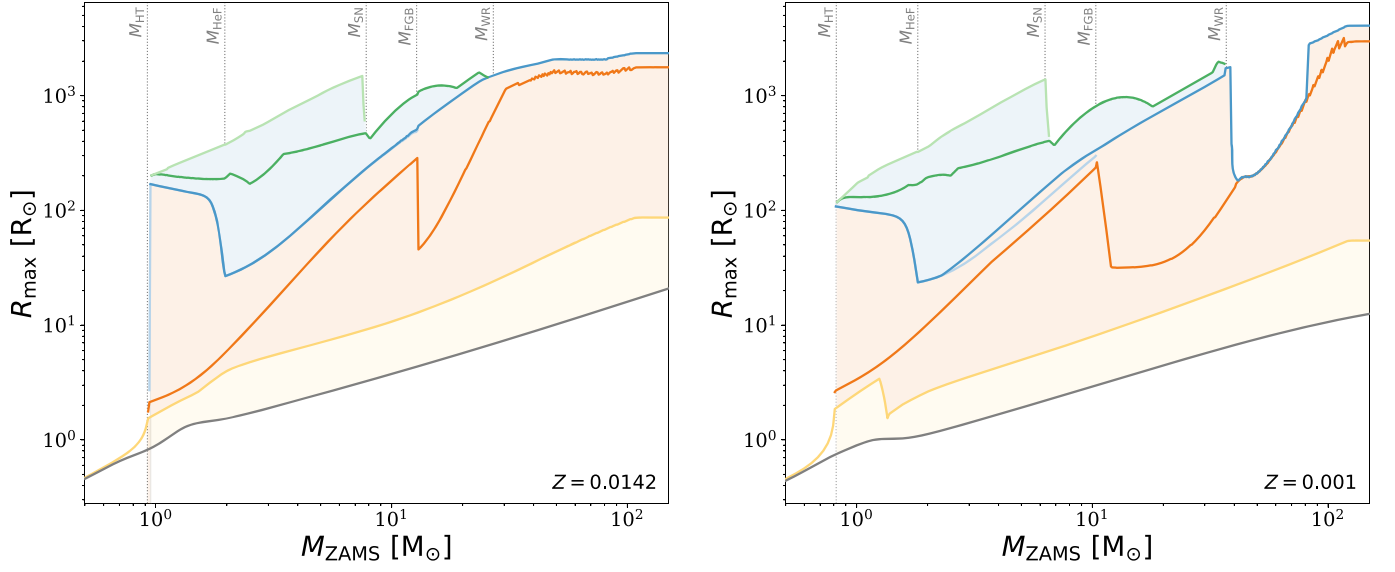


Figure 6. Maximum radial extent of stars with ZAMS masses between 0.5–150 M_{\odot} during different phases of stellar evolution, from the main sequence to the helium giant branch, using default settings. Solid lines show the maximum extent of stars during a given evolutionary phase, whose colors have the same meaning as in Figure 5. We additionally show R_{ZAMS} in gray to indicate how much the star expands during the main sequence. Note that the FGB curve is invisible when it overlaps with the CHeB curve. Shading indicates regions in which different types of mass transfer can occur due to the expansion of the donor; on the main sequence (yellow), after hydrogen exhaustion (orange) and after helium exhaustion (blue). The dashed lines indicate important transition masses in the Hurley et al. (2000) fitting formulae, where M_{HT} is the minimum mass of a star that will complete its main sequence in a Hubble time, M_{HeF} is the maximum initial mass for which helium ignites degenerately in a helium flash, M_{SN} is the mass above which a star collapses into an NS or BH, possibly with a supernova explosion, M_{FGB} is the maximum initial mass for which helium ignites on the first giant branch and M_{WR} is the minimum mass at which a star will self-strip to become a Wolf–Rayet star.

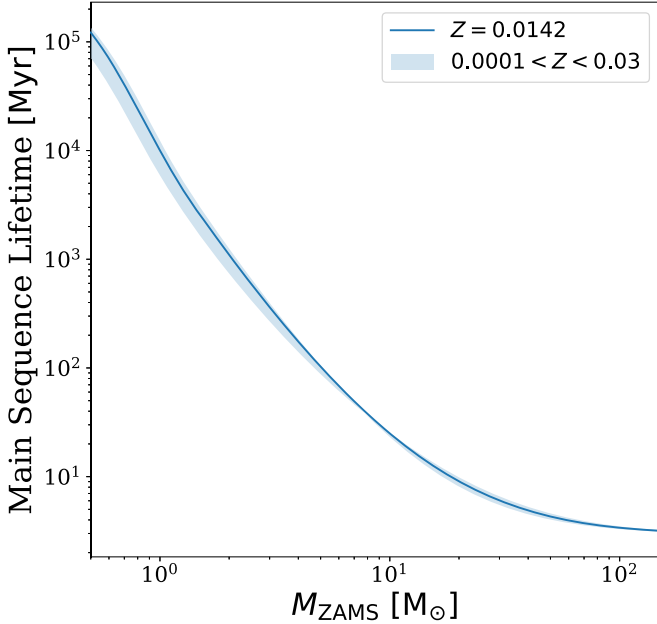


Figure 7. Main-sequence lifetimes of stars between 0.5–150 M_{\odot} using Hurley et al. (2000) fitting formulae across the range of metallicities at which these formulae can be used.

1989). This is only non-zero for luminous massive stars with $L > 4000 L_{\odot}$.

For stars on the giant branch and beyond, this model adopts the results of Kudritzki & Reimers (1978)

$$\dot{M}_{\text{KR}} = \eta \times 4 \times 10^{-13} M_{\odot} \text{ yr}^{-1} \left(\frac{L}{L_{\odot}} \right) \left(\frac{R}{R_{\odot}} \right) \left(\frac{M}{M_{\odot}} \right)^{-1}, \quad (6)$$

where η is a phenomenological scaling parameter of order unity. By default, we adopt $\eta = 0.5$ following Hurley et al. (2000).

For stars on the asymptotic giant branch they use the results of Vassiliadis & Wood (1993)

$$\dot{M}_{\text{VW}} = \min \left(10^{-11.4+0.0125(P_0-P_1)}, 1.36 \times 10^{-9} \frac{L}{L_{\odot}} \right) M_{\odot} \text{ yr}^{-1}, \quad (7)$$

where P_0 , the Mira pulsation period, is given by

$$P_0/\text{days} = \min \left[1.995 \times 10^3, 8.51 \times 10^{-3} \left(\frac{M}{M_{\odot}} \right)^{-0.9} \left(\frac{R}{R_{\odot}} \right)^{1.94} \right], \quad (8)$$

and $P_1/\text{days} = 100 \times \max(M/M_{\odot} - 2.5, 0)$.

Wolf–Rayet like wind mass loss is included for small hydrogen-envelope mass, $\mu < 1.0$, stars according to

$$\dot{M}_{\text{WR}} = 10^{-13} \left(\frac{L}{L_{\odot}} \right)^{1.5} (1 - \mu) M_{\odot} \text{ yr}^{-1}. \quad (9)$$

where the parameter μ describes the ratio of the envelope mass to the total mass, so that $\mu = 1$ on the main sequence, $0 < \mu < 1$ for stars with a developed core, and $\mu = 0$ for stripped stars with no hydrogen envelope. The full expressions for μ are given in Equation (97) in Hurley et al. (2000).

We designate post-main-sequence stars with $L > 6 \times 10^5 L_{\odot}$ and $\text{HD} \equiv 10^{-5} (R/R_{\odot}) (L/L_{\odot})^{0.5} > 1.0$ as LBV, following Humphreys & Davidson (1994). For these LBV stars Hurley et al. (2000) add an LBV-like mass loss, intended to account

for eruptive mass loss in an averaged sense

$$\dot{M}_{\text{LBV}} = 0.1(\text{HD} - 1.0)^3 \left(\frac{L/L_{\odot}}{6 \times 10^5} - 1.0 \right) M_{\odot} \text{ yr}^{-1}. \quad (10)$$

3.5.2. Belczynski Model

Belczynski et al. (2010) use a model for stellar winds based on results from Monte Carlo radiative transfer simulations of Vink et al. (2000, 2001). For stars that are not LBVs or helium stars, they define the mass-loss rate as

$$\dot{M}_{\text{B}} = \begin{cases} \dot{M}_{\text{H}}, & T/\text{K} < 12500 \\ \dot{M}_{\text{Vink,BBJ}}, & 12500 \leq T/\text{K} < 25000 \\ \dot{M}_{\text{Vink,ABJ}}, & 25000 \leq T/\text{K}, \end{cases} \quad (11)$$

where \dot{M}_{H} is the Hurley mass-loss rate defined in Section 3.5.1 and the Vink mass-loss rates are defined as

$$\log \left(\frac{\dot{M}_{\text{Vink,BBJ}}}{M_{\odot} \text{ yr}^{-1}} \right) = -6.688 + 2.210 \log(L/10^5 L_{\odot}) - 1.339 \log(M/30 M_{\odot}) - 1.601 \log(V/2.0) + 0.85 \log(Z/Z_{\odot}) + 1.07 \log(T/20000 \text{ K}), \quad (12)$$

below the bistability jump, where the ratio of the wind speed at infinity to the star's escape velocity is $V = v_{\infty}/v_{\text{esc}} = 1.3$, and as

$$\log \left(\frac{\dot{M}_{\text{Vink,ABJ}}}{M_{\odot} \text{ yr}^{-1}} \right) = -6.697 + 2.194 \log(L/10^5 L_{\odot}) - 1.313 \log(M/30 M_{\odot}) - 1.226 \log(V/2.0) + 0.85 \log(Z/Z_{\odot}) + 0.933 \log(T/40000 \text{ K}) - 10.92 [\log(T/40000 \text{ K})]^2, \quad (13)$$

above the bistability jump, where the ratio of the wind speed at infinity to the stars escape velocity is $V = v_{\infty}/v_{\text{esc}} = 2.6$. The mass-loss rate in Equations (12) and (13) above scales with metallicity as $\dot{M} \propto Z^{0.85}$, in agreement with observationally determined scaling of the mass-loss rates of O and B stars with metallicity in the Milky Way and the Magellanic Clouds (Mokiem et al. 2007).

For helium stars, Belczynski et al. (2010) assume a mass-loss rate

$$\dot{M}_{\text{B,He}} = f_{\text{WR}} \times 10^{-13} \left(\frac{L}{L_{\odot}} \right)^{1.5} \left(\frac{Z}{Z_{\odot}} \right)^m M_{\odot} \text{ yr}^{-1}, \quad (14)$$

from Hamann & Koesterke (1998), with $m = 0.86$, as given by Vink & de Koter (2005). We have introduced the phenomenological scaling parameter f_{WR} to allow the strength of WR winds to be varied (Barrett et al. 2018). Our default choice is $f_{\text{WR}} = 1$.

LBV stars have high mass-loss rates due to both line-driven winds and eruptive mass loss. The uncertainty in LBV mass-loss rates is parameterized with a scaling parameter f_{LBV} with a default value of 1.5 (Belczynski et al. 2010):

$$\dot{M}_{\text{B,LBV}} = f_{\text{LBV}} \times 10^{-4} M_{\odot} \text{ yr}^{-1}. \quad (15)$$

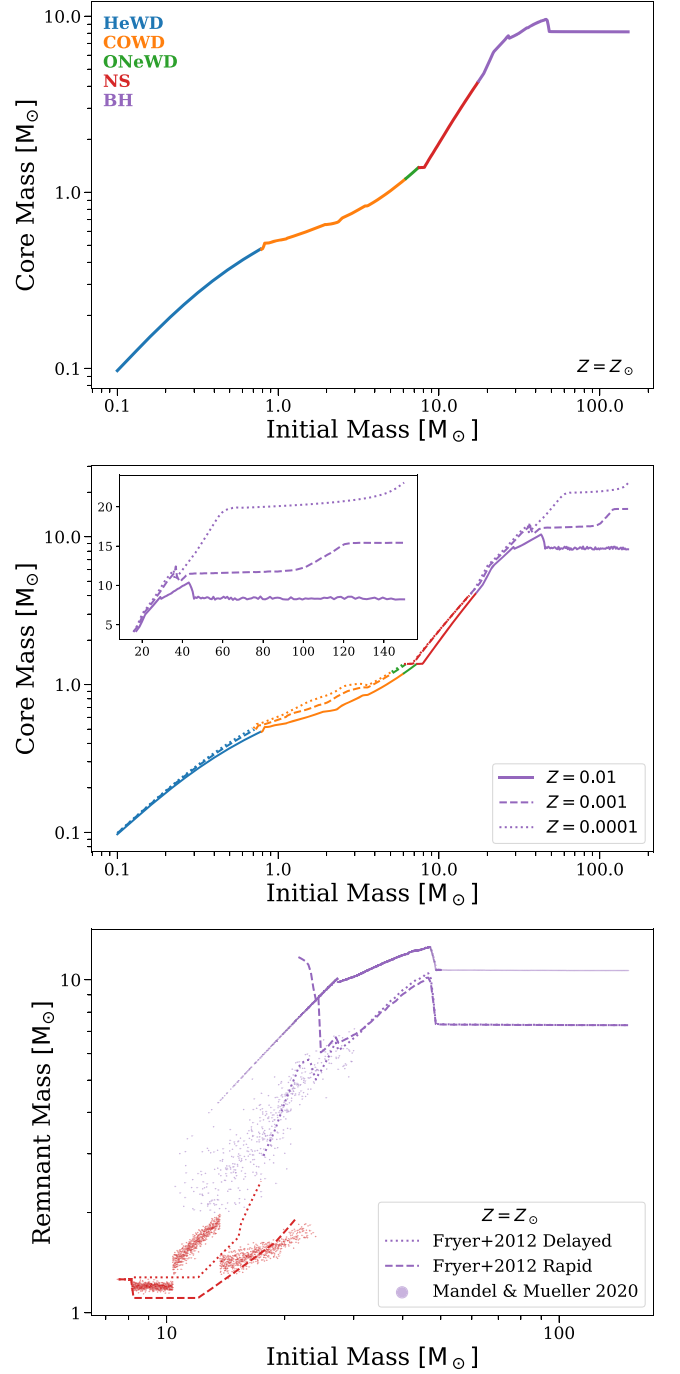


Figure 8. Top: the relation between the initial (ZAMS) mass of single stars at solar metallicity ($Z = 0.0142$) and either the WD remnant mass or the CO core mass at the moment of compact object formation for NSs and BHs, assuming the COMPAS default model, where colors denote the remnant type. Middle: the same relation at $Z = 0.01$ (solid), $Z = 0.001$ (dashed) and $Z = 0.0001$ (dotted) to show the metallicity dependence. The inset panel shows the same quantities as the main panel, but with linear axes, focusing on BH masses. Bottom: the initial–compact object mass relation at Z_{\odot} plotted for different remnant mass models (see Section 3.8.2): the *delayed* (dotted line) and *rapid* (dashed line) prescriptions from Fryer et al. (2012), and the stochastic model from Mandel & Müller (2020) (points converging to a solid line).

3.6. Treatment of the Impact of Mass Loss and Gain

The stellar tracks computed by Pols et al. (1998) assumed no mass loss. When a star loses mass during a core-burning phase

(either through stellar winds, as described in Section 3.5, or through mass transfer), its luminosity will decrease. This will extend the remaining lifetime. Meanwhile, mass gain through mass transfer (COMPAS does not account for accretion of winds from the companion) can *rejuvenate* the star. After mass gain such a star will appear younger than a single star of the same mass and age (a *blue straggler*).

For a star losing or gaining mass through either mass transfer or winds (mass loss only) on the main sequence, we follow Hurley et al. (2000; see also Tout et al. 1997) in modifying the lifetime according to

$$t' = f_{\text{rej}} \frac{t'_{\text{MS}}}{t_{\text{MS}}}, \quad (16)$$

where t and t_{MS} are the effective age and main-sequence lifetime prior to a small change in mass, and t' and t'_{MS} are the age and main-sequence lifetime of the star after a small amount of mass loss/gain. Mass changes for helium main-sequence stars are treated by analogy with the above equation, with the main-sequence lifetimes t_{MS} and t'_{MS} replaced with t_{HeMS} and t'_{HeMS} , respectively (Hurley et al. 2000).

The prefactor f_{rej} is unity for all mass-losing stars (and for low-mass $M \leq 0.7 M_{\odot}$ main-sequence stars, stellar type 0), while it is taken to be the ratio of the mass before/after mass gain for main-sequence stars initially more massive than $0.7 M_{\odot}$ (Belczynski et al. 2008) and helium main-sequence stars. The ages of Hertzsprung gap stars are updated following mass changes as described in Hurley et al. (2000). For giants with clearly decoupled cores and envelopes, we assume that changes to the envelope (such as mass loss/gain) do not affect the remaining lifetime. See Schneider et al. (2015) and references therein for more details and possible improvements.

3.7. Stellar Remnants

Standard stellar evolution theory predicts that low and intermediate mass stars (with initial masses $\lesssim 8 M_{\odot}$) typically end their lives as WDs (Section 3.7.1), while more massive stars end their lives by collapsing into NSs and BHs (Section 3.7.2). We show the relation between initial masses, core masses and remnant masses of stars evolved under default COMPAS assumptions in Figure 8.

3.7.1. White Dwarfs

We distinguish between three different types of WDs based on their mass and composition, following Hurley et al. (2000). Stars that lose their envelopes prior to helium ignition leave behind helium white dwarfs (HeWDs), while those that lose their envelopes after core-He exhaustion leave behind either carbon–oxygen white dwarfs (COWDs) or oxygen–neon white dwarfs (ONeWDs) depending on their core masses upon reaching the base of the asymptotic giant branch. Larger core masses are associated with higher temperatures that allow carbon to fuse, forming oxygen–neon or oxygen–neon–magnesium cores. We assume that helium core masses below $1.6 M_{\odot}$ at the base of the asymptotic giant branch lead to COWD formation, while core masses above that lead to ONeWD formation. For our default model, we find that single stars with initial masses $\lesssim 0.8 M_{\odot}$ form HeWDs (though the evolutionary timescale for these stars to evolve is longer than a Hubble time), while heavier stars with initial masses up to $\approx 7 M_{\odot}$ form COWDs. Only stars in a narrow mass range

of $\approx 7\text{--}8 M_{\odot}$ form ONeWDs (see upper panel of Figure 8). The boundary between stars that form WDs and those that form NSs/BHs is uncertain (see, for example, Doherty et al. 2017, for further discussion). WDs have masses $\lesssim 1.4 M_{\odot}$ (the Chandrasekhar mass) in our model. We determine the radius of WDs following Tout et al. (1997) and Hurley et al. (2000). WDs cool as they age (Mestel 1952). We model the luminosity of WDs using the Mestel cooling track given in Equation (90) in Hurley et al. (2000). By default we assume that WDs do not receive any kick during formation (but see El-Badry & Rix 2018 for a discussion of evidence for small $\sim 1 \text{ km s}^{-1}$ recoil velocities associated with WD formation).

3.7.2. Neutron Stars and Black Holes

Stars with initial masses more than $\sim 8 M_{\odot}$ collapse into an NS or a BH at the end of their lives. This collapse may be accompanied by a supernova explosion. This collapse may be accompanied by a supernova explosion. Asymmetry in the supernova may give the remnant a substantial momentum boost, commonly known as a *natal kick* (see Section 3.9). The mass of the supernova remnant (and by extension its stellar type), as well as the natal kick all depend on which kind of supernova it undergoes. In COMPAS we distinguish between several different types of supernovae, which are discussed in Section 3.8.

COMPAS distinguishes NSs from BHs by the remnant mass; the default value of the maximum NS mass is $2.5 M_{\odot}$, following Fryer et al. (2012).

Figure 8 shows the core mass and remnant mass as a function of initial mass for single stars in the mass range $0.1\text{--}150 M_{\odot}$ in the COMPAS default model. The top panel of Figure 8 shows the mass ranges in which each type of stellar remnant is formed at solar metallicity. The middle panel of Figure 8 shows how the initial mass–core mass relation varies with metallicity, while the bottom panel shows how the relation depends on which remnant mass prescription is used for solar metallicity. This figure can be compared to results from Belczynski et al. (2010) and Banerjee et al. (2020).

By default, in COMPAS we follow Hurley et al. (2000) in assuming all NSs have a radius of 10 km. We also include the possibility of defining the NS radius as a function of its mass $R_{\text{NS}}(M_{\text{NS}})$, as expected from the equation of state. Currently, the NS equation of state from Akmal et al. (1998) is implemented in COMPAS, which gives NS radii of 11–12 km for NSs in the astrophysically relevant mass range $1\text{--}2.4 M_{\odot}$. The maximum NS mass predicted by this equation of state is $2.4 M_{\odot}$.

The NS moment of inertia is assumed to follow the “universal” (equation of state insensitive) relation given by Lattimer & Schutz (2005). The luminosity of NSs is estimated following Hurley et al. (2000).

For output purposes only, the “radius” of a BH is given by its Schwarzschild radius

$$R_{\text{BH}} = \frac{2GM}{c^2} \approx 4.24 \times 10^{-6} R_{\odot} \frac{M}{M_{\odot}} \quad (17)$$

and we follow Hurley et al. (2000) in arbitrarily setting the BH luminosity to $10^{-10} L_{\odot}$.

Pulsar evolution is implemented in COMPAS as described in Chattopadhyay et al. (2020, 2021). We assign a spin period and an initial magnetic field to each newly born NS. We provide several options for the initial distribution of pulsar spin periods and magnetic fields, see Chattopadhyay et al. (2020) for details.

The evolution of the pulsar spin period and spindown rate are followed as a function of time, assuming the canonical magnetic dipole model for a pulsar. In this model, pulsars spindown over time due to magnetic braking, but may be spun up again (or recycled) through mass accretion. Our approach closely follows the methodology of Osłowski et al. (2011), Kiel et al. (2008), and Faucher-Giguere & Kaspi (2006; see also Ye et al. 2019). Other pulsar properties, such as the pulsar luminosity or beaming fraction, are not directly computed by COMPAS, but can easily be modeled in postprocessing (see Chattopadhyay et al. 2020, 2021, for details). Pulsar evolution is optional in COMPAS and is disabled in the default model.

BHs are assumed to be nonspinning. However, the spins of BHs have been modeled by postprocessing COMPAS data in a number of papers (Bavera et al. 2020; Chattopadhyay et al. 2021).

3.8. Supernova Types

In COMPAS we distinguish between several different types of supernovae. In the following, we describe the types of supernovae we model and the conditions under which each type of supernova is assumed to occur. COMPAS records whether the supernova progenitor star has a hydrogen-rich envelope, allowing for a crude estimation of whether it would appear observationally as a type I or II supernova.

3.8.1. Electron-capture Supernovae

In COMPAS we assume that a star undergoes an electron-capture supernova (ECSN; Miyaji et al. 1980; Nomoto 1984, 1987; Ivanova et al. 2008) if it has a helium core mass in the range $1.6\text{--}2.25 M_{\odot}$ (Hurley et al. 2002) at the base of the asymptotic giant branch, and the carbon–oxygen core mass reaches a threshold of $1.38 M_{\odot}$. In our default model, this corresponds to a ZAMS mass range of $7.5\text{--}8.1 M_{\odot}$ for single stars at Z_{\odot} .

The mass range of stars that undergo ECSNe is somewhat uncertain and model dependent. For example, Podsiadlowski et al. (2004) argued that a more realistic range of helium core masses leading to ECSNe is $1.4\text{--}2.5 M_{\odot}$. Andrews et al. (2015) and Vinciguerra et al. (2020) use different core mass ranges for ECSNe ($2\text{--}2.5 M_{\odot}$ and $1.83\text{--}2.25 M_{\odot}$, respectively, where the latter is based on Fryer et al. (2012), which could better reproduce observations of NSs). Willcox et al. (2021) argued that the (ZAMS) mass range of (effectively) single stars undergoing ECSNe cannot be wider than $0.2 M_{\odot}$ to avoid overproducing low velocity pulsars, but ECSNe could be more common in binaries.

If a star undergoes an electron-capture supernova, we set its remnant to be an NS with a mass of $1.26 M_{\odot}$, as an approximation to the solution of Equation (8) in Timmes et al. (1996), assuming a baryonic mass of $1.38 M_{\odot}$.

Massive oxygen–neon WDs (ONeWDs) close to the Chandrasekhar mass can accrete enough mass to undergo an accretion-induced collapse (AIC) to an NS (Nomoto & Kondo 1991). While AIC is nominally possible in COMPAS when the mass of a ONeWD reaches $1.38 M_{\odot}$, when the ECSN prescription is followed for the remnant mass and natal kick, this is based on a very simplistic implementation of accretion onto WDs.

3.8.2. Core-collapse Supernovae

Stars with helium core masses greater than $2.25 M_{\odot}$ at the base of the asymptotic giant branch undergo core-collapse

supernovae (CCSNe) in COMPAS, if/when their carbon–oxygen core mass reaches the threshold given by Hurley et al. (2000), where we replace their Chandrasekhar mass threshold with $1.38 M_{\odot}$.

There is still a great deal of uncertainty regarding the mechanism of CCSNe, including which stars explode, how they explode, and what the properties of their remnants are (see Müller 2020 and Burrows & Vartanyan 2021 for recent reviews). Some recent supernova simulations predict that whether a supernova is successful and leads to an explosion, or fails and leads to an implosion, is a nonmonotonic function of a star’s initial mass (Ugliano et al. 2012; Sukhbold & Woosley 2014; Nakamura et al. 2015; Ertl et al. 2016; Sukhbold & Adams 2020). COMPAS uses simple parameterized models (described below) to relate the properties of supernova remnants to their progenitor stars. We attempt to parameterize some of this uncertainty by including several different models.

By default, COMPAS uses the *delayed* supernova remnant mass prescription from Fryer et al. (2012) to map the carbon–oxygen core masses of stars to compact object remnant masses during core-collapse supernova events. An alternative *rapid* prescription assumes supernova explosions occur within 250 ms (compared to longer timescales assumed for the delayed model) and reproduces, by construction, a mass gap between NSs and BHs. Mandel & Müller (2020) proposed a model for compact object masses and kicks which is stochastic, with both NS and BH formation possible in certain regions of parameter space; this model was implemented in COMPAS in Mandel et al. (2021). Schneider et al. (2021) predict that the history of mass transfer impacts the remnant mass, and we include their remnant mass prescription. We also include the slightly older remnant mass prescriptions from Hurley et al. (2000) and Belczynski et al. (2008), which define the remnant mass as a piecewise function or linear function, respectively, of the progenitor carbon–oxygen core mass; these models are provided for historical consistency reasons, but are somewhat outdated.

We convert the baryonic mass of the remnant to a gravitational mass using Equation (13) of Fryer et al. (2012) for NSs. For BHs, the gravitational mass is assumed to be $0.1 M_{\odot}$ less than the baryonic mass to account for mass lost in neutrinos in the default prescription (Stevenson et al. 2019). This amount can be adjusted, or, alternatively, a fixed fraction of the mass can be lost in neutrinos during BH formation as in Equation (14) of Fryer et al. (2012).

We show the difference in the initial-final remnant mass relation between the two models from Fryer et al. (2012) and the stochastic model from Mandel & Müller (2020) in the bottom panel of Figure 8.

3.8.3. Ultra-stripped Supernovae

Mass transfer from a helium star that re-expands after core helium burning (so-called “case BB mass transfer”; Delgado & Thomas 1981; Tauris et al. 2015) in short-period binaries leads to severe stripping of the donor, leaving behind a helium envelope with mass $\lesssim 0.1 M_{\odot}$. If the remaining stellar core is sufficiently massive to undergo core collapse, then we say that it undergoes an ultra-stripped supernova (USSN; Tauris et al. 2013, 2015). Due to the lack of envelope, USSNe remnants are NSs with characteristically lower mass, and may receive smaller natal kicks than typical NSs (Suwa et al. 2015; Moriya

et al. 2017; Müller et al. 2018). We discuss kicks further in Section 3.9. By default in COMPAS we assume that case BB mass transfer is always stable (see Vigna-Gómez et al. 2018) and removes the entire helium envelope but none of the underlying carbon–oxygen core.

3.8.4. Pair-instability Supernovae

Stars with helium cores in the mass range $\sim 50\text{--}150 M_{\odot}$ are believed to become unstable as a result of electron–positron pair production (Fowler & Hoyle 1964; Barkat et al. 1967; Woosley 2017; Farmer et al. 2019). This causes the radiation pressure support in the core to drop, causing the core to contract. As it contracts, the temperature increases, triggering explosive oxygen burning. This may reverse the contraction and completely unbind the star in a pair-instability supernovae (PISNe) explosion, leaving no remnant behind (Fowler & Hoyle 1964; Barkat et al. 1967; Fraley 1968; Kozyreva et al. 2014a, 2014b, 2017; Takahashi 2018; Leung et al. 2019; Woosley 2019). BH formation is expected again above a helium core mass of $\sim 150 M_{\odot}$ (Woosley et al. 2002; Woosley 2019). In addition, it is theoretically well established that stars with helium core masses in the range $\sim 30\text{--}60 M_{\odot}$ lead to pulsational PISNe (e.g., Yoshida et al. 2016; Spera & Mapelli 2017; Woosley 2017; Takahashi 2018; Farmer et al. 2019; Marchant et al. 2019; Renzo et al. 2020), where material from the star is ejected in several supernova-like pulses, while the star returns to equilibrium between each pulse, and eventually undergoes an iron core collapse to form a BH. Together, these effects lead to a dearth of BHs in the mass range $\sim 45\text{--}130 M_{\odot}$ and a possible excess in the $\sim 35\text{--}45 M_{\odot}$ mass range with the current COMPAS default prescription.

The implementation of PISNe in COMPAS is discussed in detail in Stevenson et al. (2019). In brief, by default stars with helium core masses in the range between 35 and $60 M_{\odot}$ lose mass through pulsational PISNe prior to collapse, while those with helium core masses between 60 and $135 M_{\odot}$ explode in PISNe and leave no remnants behind. We use fits based on results from Marchant et al. (2019) in the COMPAS default model for the relation between the helium core mass and the final presupernova mass in the pulsational PISNe regime. In addition, COMPAS also provides the simple model from Belczynski et al. (2016a) to allow for comparison with StarTrack models, along with additional models based on detailed results from Woosley (2017) and Farmer et al. (2019).

3.9. Supernova Natal Kicks

Galactic pulsars are observed to have large proper motions, from which a distribution of their velocities is inferred (e.g., Gunn & Ostriker 1970; Lyne & Lorimer 1994; Hansen & Phinney 1997; Arzoumanian et al. 2002; Hobbs et al. 2005; Beniamini & Piran 2016; Verbunt et al. 2017). The high velocities are attributed to significant asymmetries in the supernova explosions which “kick” the pulsars, though the exact mechanism is uncertain and may be attributed to either hydrodynamic effects (e.g., Janka & Müller 1994; Burrows & Hayes 1996; Wongwathanarat et al. 2013) or neutrino emission (Woosley 1987; Bisnovatyi-Kogan 1993; Socrates et al. 2005; Nagakura et al. 2019). See Lai et al. (2001) for a broad overview of natal kicks.

By default, for NSs we draw the the natal-kick magnitudes from a Maxwell–Boltzmann distribution

$$p(v_{\text{kick}}|\sigma_{\text{kick}}) = \sqrt{\frac{2}{\pi}} \frac{v_{\text{kick}}^2}{\sigma_{\text{kick}}^3} \exp\left(-\frac{v_{\text{kick}}^2}{2\sigma_{\text{kick}}^2}\right), \quad (18)$$

with root-mean-square 1D velocity σ_{kick} (i.e., root-mean-square speed of $\sqrt{3}\sigma_{\text{kick}}$). For CCSNe, we assume that $\sigma_{\text{kick}} = \sigma_{\text{CCSN}} = 265 \text{ km s}^{-1}$ (Hobbs et al. 2005). ECSNe and USSNe are expected to have smaller kicks than standard iron core-collapse supernovae (e.g., Suwa et al. 2015; Gessner & Janka 2018; Müller et al. 2019). By default, we assume $\sigma_{\text{ECSN}} = \sigma_{\text{USSN}} = 30 \text{ km s}^{-1}$ (Vigna-Gómez et al. 2018). These lower natal kicks for ECSN and USSN follow Pfahl et al. (2002a) and Podsiadlowski et al. (2004), which are motivated by the subset of DNSs and NS–binary systems with low velocities and small eccentricities (Briskin et al. 2002; Schwab et al. 2010; Beniamini & Piran 2016; Tauris et al. 2017), as well as NS retention fractions in globular clusters (e.g., Pfahl et al. 2002b).

Several authors have proposed that NS kicks should be proportional to the amount of ejecta, and inversely proportional to the remnant mass (Bray & Eldridge 2016, 2018; Giacobbo & Mapelli 2020; Mandel & Müller 2020). A scaling with ejecta mass would naturally account for reduced kicks in USSNe with low ejecta mass. In COMPAS we have implemented the fits of this form from Bray & Eldridge (2018) and Mandel & Müller (2020), where the latter model self-consistently predicts both the remnant mass and natal kick.

COMPAS also includes a model for remnant masses and kicks based on the 1D parameterized supernova simulations of Müller et al. (2016; see Vigna-Gómez et al. 2018, for details).

We further provide the option to use a uniform distribution of kick velocities up to some maximum $v_{\text{kick}}^{\text{max}}$, as well as kicks fixed at a specific value.

Whether BHs also receive natal kicks, and what their magnitudes are is an open astrophysical question. There is some evidence, both theoretical and observational, that BHs receive smaller kicks than NSs (see, e.g., Janka 2013; Mandel 2016; Repetto et al. 2017; Atri et al. 2019).

COMPAS currently includes four different models for BH natal kicks: “full,” “reduced,” our default model “fallback,” and “zero.” In the “full” model, we assume that BHs receive the full kick drawn from Equation (18), where by default we assume $\sigma_{\text{kick}} = \sigma_{\text{CCSN}}$ for BHs. In both the “reduced” and the “fallback” models, we calculate the intensity of the kick velocity imparted to newly born BHs from the kick that a NS would have received according to Equation (18) with $\sigma_{\text{kick}} = \sigma_{\text{CCSN}}$. In the “reduced” model, we assume that NSs and BHs receive the same *momentum* during the explosion, such that the kick velocity of a BH should be rescaled according to

$$v_{\text{BH}} = \frac{M_{\text{NS}}}{M_{\text{BH}}} v_{\text{NS}}, \quad (19)$$

where M_{NS} is taken to be $1.4 M_{\odot}$. In the “fallback” model, we scale the BH kick by the fraction of mass falling back onto the proto-NS f_{fb} (Fryer et al. 2012)

$$v_{\text{BH}} = v_{\text{NS}}(1 - f_{\text{fb}}). \quad (20)$$

Note that unlike Fryer et al. (2012), we apply Equation (20) even if the amount of mass falling back is less than $M = 0.2 M_{\odot}$. In COMPAS, by default we apply Equation (20) to all compact objects when using this prescription. In the “zero” kicks model, BHs receive no kick during their collapse.

By default, we assume the supernova kick angle is drawn isotropically from the unit sphere in the rest frame of the supernova progenitor. However, there is some tentative observational evidence for spin-kick alignment in pulsars (e.g., Lai et al. 2001; Johnston et al. 2005; Noutsos et al. 2012; Yao et al. 2021), which may indicate that kicks are preferentially aligned to the spin axis of the progenitor. We provide various alternative models for preferential kick directionality, including along the progenitor spin axis (or in a finite cone around it), or within the progenitor spin plane (or in a wedge around it). We describe the impact of the supernova on the orbit of a binary in Section 4.3.

4. Binary Stellar Evolution

Interacting binaries are the core case of study for COMPAS. Mass transfer is arguably the most important process in interacting binaries, modifying the component stars and the orbital properties (Podsiadlowski et al. 1992; Podsiadlowski 2010). Binary evolution can lead to stellar mergers, disruption, or DCO formation.

A binary in COMPAS is parameterized by the orbital properties: the component masses of the primary M_1 and secondary M_2 , the semimajor axis a , and eccentricity e . The orbital angular momentum of a binary with nonrotating stars is

$$J_{\text{orb}} = \mu \sqrt{GM_{\text{tot}} a (1 - e^2)}, \quad (21)$$

where $M_{\text{tot}} = M_1 + M_2$ and $\mu = M_1 M_2 / M_{\text{tot}}$ is the reduced mass. The effects of binary interactions on the stellar components, such as mass transfer and rejuvenation, are considered within our SSE framework (Section 3). We currently only account for stellar rotation in the context of CHE systems (Section 3.4). In the absence of rotation and tides, the binary can be treated as a two-body problem in the point mass approximation.

In this Section we present the details of our treatment of BSE. In Section 4.1 we discuss stellar winds in the context of binaries. In Section 4.2 we present our implementation of mass transfer. In Section 4.3 we describe the effect of supernovae on the orbit of the binary. In Section 4.4 we describe our implementation of gravitational radiation. Finally, in Section 4.5 we briefly discuss the main caveats in our implementation of binary evolution.

4.1. Wind Mass Loss (Binary System)

In Section 3.5 we presented the prescriptions and parameterization of stellar wind mass-loss rates in COMPAS. Here we present the effect of wind mass loss on the orbit of the binary system.

We consider the case of gradual mass loss ($M/\dot{M} \gg P_{\text{orb}}$) in which material rapidly leaves the system with the specific angular momentum of the mass-losing star (wind velocities are fast compared to the orbital velocity). We assume that the fast winds are emitted spherically symmetrically from the star’s surface (Huang 1956). This is known as the *Jeans mode* or *fast winds*

mode (Huang 1963). In the case, the orbit widens according to

$$\frac{\dot{a}}{a} = -\frac{\dot{M}_{\text{tot}}}{M_{\text{tot}}}, \quad (22)$$

which can be simplified as $aM_{\text{tot}} = \text{constant}$, while eccentricity is unchanged (Dosopoulou & Kalogera 2016). Winds can thus be considered as an extreme case of nonconservative mass transfer (Section 4.2).

Currently we do not consider wind accretion (e.g., Bondi & Hoyle 1944), wind RLOF (Mohamed & Podsiadlowski 2007; Hirai & Mandel 2021), or wind interaction with the companion (Brookshaw & Tavani 1993; Schröder et al. 2021).

4.2. Mass Transfer

The physics and timescales involved in mass exchange are broad, complex, and their parameterizations can be convoluted. In COMPAS, we use a simplified approach to this complicated problem. Our approach is similar to that of Belczynski et al. (2002, 2008), Hurley et al. (2002), and Postnov & Yungelson (2014), among others. We distinguish between a donor (subscript d) and an accretor (subscript a). The donor is the star that transfers (and loses) mass, while the accretor gains mass. The accretor can be a star or a compact object, and can fully retain the transferred mass (conservative mass transfer) or only a fraction of it (nonconservative mass transfer). If the mass transfer is nonconservative, i.e., some mass is lost from the binary, there is a change in the total angular momentum of the binary. We follow the orbital evolution of the binary through a mass transfer episode by taking the time derivative of Equation (21) and rearranging it as

$$\frac{\dot{a}}{a} = 2 \frac{\dot{J}_{\text{orb}}}{J_{\text{orb}}} - 2 \frac{\dot{M}_d}{M_d} - 2 \frac{\dot{M}_a}{M_a} + \frac{\dot{M}_d + \dot{M}_a}{M_d + M_a} + \frac{2e\dot{e}}{1 - e^2}. \quad (23)$$

The default COMPAS assumption is that the binary is instantly circularized to periastris, $r_p = a(1 - e)$, at the onset of RLOF. COMPAS options allow circularization with angular momentum conservation (at a separation of the semilatus rectum, $a(1 - e^2)$) or mass transfer with unchanged eccentricity.

We parameterize the fraction of mass lost by the donor which is accreted by the accretor with a factor β :

$$\dot{M}_a = -\beta \dot{M}_d, \quad (24)$$

with $0 \leq \beta \leq 1$. We parameterize the change in angular momentum by assuming the nonaccreted matter leaves the system with γ times the specific orbital angular momentum, i.e., $\dot{J}_{\text{orb}}/\dot{M} = \gamma J_{\text{orb}}/M$. Following these assumptions we can rewrite Equation (23) as²²

$$\frac{\dot{a}}{a} = -2 \frac{\dot{M}_d}{M_d} \left[1 - \beta \frac{M_d}{M_a} - (1 - \beta) \left(\gamma + \frac{1}{2} \right) \frac{M_d}{M_d + M_a} \right], \quad (25)$$

which is the equation we use to solve for the orbital evolution during a mass transfer episode. Note that fully nonconservative mass transfer ($\beta = 0$), where mass is lost with the specific

²² See the educational lecture notes on binary evolution by Onno Pols: http://www.astro.ru.nl/~onnop/education/binaries_utrecht_notes/.

angular momentum of the donor star ($\gamma = M_a/M_d$), is equivalent to fast wind mass loss from Section 4.1.

Before solving for the orbital evolution during a mass transfer phase, we first need to determine if mass transfer will occur (Section 4.2.1) and, if so, whether the mass transfer episode will be dynamically stable (Sections 4.2.2 and 4.2.3). If the mass transfer episode is dynamically unstable, it will lead to a common envelope phase (Section 4.2.4).

4.2.1. Roche-lobe Overflow

A mass transfer phase can be initiated either by the radial expansion of a star as a consequence of stellar evolution or by a decrease in the binary separation. The star overflows its Roche lobe and the surface material is transferred from the donor to the companion through the first Lagrangian point. The first Lagrangian point is the juncture between the two Roche lobes, which are the regions that contain the gravitationally bound material around each star. In COMPAS we follow Eggleton (1983) and approximate the radius of the donor's Roche lobe normalized by the separation as

$$r_{\text{RL}} = R_{\text{RL}}/a = 0.49 \frac{q_{\text{RL}}^{2/3}}{0.6q_{\text{RL}}^{2/3} + \ln(1 + q_{\text{RL}}^{1/3})}, \quad (26)$$

with $q_{\text{RL}} = M_d/M_a$. Equation (26) assumes point-like masses in a circular orbit. The Roche lobe is generally shaped like a teardrop, but here the Roche lobe radius is defined as the radius of a sphere which has the same volume as the Roche lobe. The condition for RLOF, and therefore for initiating mass transfer, is when the radius of the star is larger than the Roche radius at periaapsis, i.e., when $R > R_{\text{RL}}(1 - e)$.

4.2.2. Stability Criteria

When the condition for RLOF is satisfied, we need to determine if the mass transfer episode will be dynamically stable or lead to a common envelope event. In COMPAS, the stability of the mass transfer phase is determined based on approximations to the mass–radius relationships $\zeta \equiv d \ln R/d \ln M$ (see, e.g., Soberman et al. 1997). Namely, the response of the radius of the donor star to mass loss $\zeta_* \equiv d \ln R_*/d \ln M$ is compared to the response of the Roche-lobe radius $\zeta_{\text{RL}} \equiv d \ln R_{\text{RL}}/d \ln M$ to mass transfer (Paczynski & Sienkiewicz 1972; Hjellming & Webbink 1987; Soberman et al. 1997). If $\zeta_* \geq \zeta_{\text{RL}}$, then the mass transfer episode is assumed to be stable, otherwise, mass transfer is assumed to lead to a common envelope phase.

We approximate the value of ζ_* based on stellar types (Section 3.2). We assume $\zeta_* = 2$ for main-sequence and HeMS stars and $\zeta_* = 6.5$ for HG stars, as implemented in Vigna-Gómez et al. (2018), based on typical values from Ge et al. (2015). These ζ_* values translate into critical mass ratios for stable mass transfer of $M_d/M_a < 1.72$ ($M_d/M_a < 2.25$) for fully conservative (fully nonconservative) mass transfer from main-sequence donors and $M_d/M_a < 3.83$ ($M_d/M_a < 4.58$) for HG donors. For stellar types HG, FGB, CHeB, EAGB, and TPAGB (where we use these stellar types, defined in Section 3.2, as loose proxies for having a convective envelope, but see, e.g., Klencki et al. 2021) we follow Soberman et al. (1997) in the

form

$$\zeta_{\text{SPH}} = \frac{2}{3} \left(\frac{m_{\text{SPH}}}{1 - m_{\text{SPH}}} \right) - \frac{1}{3} \left(\frac{1 - m_{\text{SPH}}}{1 + 2m_{\text{SPH}}} \right) - 0.03m_{\text{SPH}} + 0.2 \left[\frac{m_{\text{SPH}}}{1 + (1 - m_{\text{SPH}})^{-6}} \right], \quad (27)$$

where $m_{\text{SPH}} = M_{\text{core}}/M$ and M_{core} is the core mass as defined by Hurley et al. (2000). In COMPAS, we consider stripped post-helium-burning stars as a special case and assume by default that any mass transfer episode from HeHG and HeGB stellar types is always stable. This is in agreement with the expected outcome of mass transfer episodes from stripped stars onto NSs or BHs as suggested by Tauris et al. (2013, 2015). We currently do not model mass transfer from white dwarf donors (HeWD, COWD, and ONeWD).

The Roche-lobe mass–radius exponent ζ_{RL} depends on the accreted mass fraction β and the specific angular momentum that nonaccreted mass removes from the system (see Section 4.2.3 to see how we determine these). We follow Soberman et al. (1997) and Woods et al. (2012) in rewriting

$$\zeta_{\text{RL}} = \frac{d \ln R_{\text{RL}}}{d \ln M} = \frac{\partial \ln a}{\partial \ln M_d} + \frac{\partial \ln r_{\text{RL}}}{\partial \ln q_{\text{RL}}} \frac{\partial \ln q_{\text{RL}}}{\partial \ln M_d}, \quad (28)$$

where the terms are taken from Equation (25) and the partial derivative of Equation (26).

4.2.3. Stable Mass Transfer

The amount of mass transferred during a dynamically stable mass transfer episode is calculated depending on the stellar type of the donor (Section 3.2). Broadly, we distinguish between stars that have a clear core/envelope separation (HG, FGB, CHeB, EAGB, TPAGB, HeHG, and HeGB) and those which do not (MS and HeMS). We do not consider other donor types.

For donor stars with a clear core/envelope separation we transfer their entire envelope. For donor stars without a clear core/envelope separation, we calculate and remove the minimal mass necessary in order to have the donor fit within its Roche lobe. Numerically, we accomplish this by using a root-finder with specified tolerances. We compute the accreted mass fraction β once, at the start of the mass transfer phase, as follows.

We compute the donor and accretor mass transfer rates. For the donor, we assume a thermal timescale mass transfer rate

$$\dot{M}_d = M_d/\tau_{\text{KH},d}. \quad (29)$$

For the accreting object, the maximum accretion rate is limited depending on its stellar type

$$\dot{M}_a = \begin{cases} \dot{M}_{\text{KH},a} & \text{if stellar accretor,} \\ \dot{M}_{\text{edd}} & \text{if compact object accretor.} \end{cases} \quad (30)$$

In Equation (30), the thermal mass accretion rate is given by

$$\dot{M}_{\text{KH},a} = C \cdot M_a/\tau_{\text{KH},a}, \quad (31)$$

where the factor $C = 10$ (default value) is assumed to take into account the expansion of the star due to mass transfer, following Paczynski & Sienkiewicz (1972), Neo et al. (1977), Hurley et al. (2002) and Schneider et al. (2015). Meanwhile,

the Eddington-limited accretion rate is given by

$$\dot{M}_{\text{edd}} = 1.5 \times 10^{-8} \frac{R_*}{10 \text{ km}} \frac{M_\odot}{\text{yr}}, \quad (32)$$

where for a black hole the radius R_* is given by the Schwarzschild radius as in Equation (17). The Eddington accretion rate assumptions in COMPAS are flexible and can be change to a user-specified function (see van Son et al. 2020 for more details).

By comparing the donor and accretor mass transfer rates, we can determine how conservative the mass transfer episode is. Only for main-sequence (MS and HeMS) and Hertzsprung gap (HG and HeHG) stars, mass accretion leads to stellar rejuvenation (Section 3.6) as the accretor star transitions to a more massive and less evolved stellar track (Tout et al. 1997; Hurley et al. 2002; Belczynski et al. 2008). For fully conservative mass transfer, i.e., $\beta = 1$, there is no angular momentum drained from the binary and Equation (25) simplifies to $M_d^2 M_a^2 a = \text{constant}$. For nonconservative mass transfer, i.e., $\beta < 1$, the nonaccreted mass is lost, by default, through *isotropic re-emission* from the vicinity of the accreting star (e.g., Masevitch & Yungelson 1975; Bhattacharya & van den Heuvel 1991; Soberman et al. 1997). Isotropic re-emission corresponds to $\gamma = M_d/M_a$.

We briefly point out some alternatives from the default mass transfer model which the user can choose in COMPAS. The user can specify a fixed value for β , which enforces that a fraction β of the mass transferred by the donor is accreted, except for Eddington-limited accretion. The value of γ can also be changed. We have mentioned the Jeans ($\gamma = M_a/M_d$) mass-loss mode in the context of winds, but we also include the user-defined possibility of choosing these mass-loss modes in semiconservative and fully nonconservative mass transfer episodes. COMPAS also includes a mode of nonconservative mass transfer that represents mass loss via a circumbinary ring as an option (see, e.g., Soberman et al. 1997). In this case, the nonaccreted mass carries a specific angular momentum $\gamma = \sqrt{a_{\text{ring}}/a} M/\mu = \sqrt{2} M/\mu$ for a ring at radius $a_{\text{ring}} = 2a$.

4.2.4. Common Envelope Phase (Dynamically Unstable Mass Transfer)

In COMPAS, dynamically unstable mass transfer occurs if $\zeta_* < \zeta_{\text{RL}}$ or if both stars simultaneously experience RLOF (see Section 4.2.6 for an exception for CHE binaries). Dynamically unstable mass transfer leads to a CE phase. In this phase, the binary is engulfed in a shared envelope and experiences gas drag, which causes a dynamical timescale inspiral (Paczynski 1976; Podsiadlowski 2001; Ivanova et al. 2013). CE events are thought to be especially relevant for the formation of DCOs in tight orbits (van den Heuvel 1976; Ivanova et al. 2013).

In COMPAS we follow the energy formalism in the form of the $\alpha_{\text{CE}}\text{-}\lambda$ prescription to estimate the post-CE orbital separation (Webbink 1984; de Kool 1990). In the $\alpha_{\text{CE}}\text{-}\lambda$ prescription the initial (pre-CE) binding energy of the donor is equated to the orbital energy reservoir

$$E_{\text{bind}} = \alpha_{\text{CE}} \times \Delta E_{\text{orb}}, \quad (33)$$

where ΔE_{orb} is the difference between the binary orbital energies before and after the CE phase and α_{CE} is a user-specified efficiency factor which parameterizes the fraction of

the orbital energy that is used to unbind the CE. The default value is $\alpha_{\text{CE}} = 1.0$.

The value of the binding energy of the envelope depends on the location of the envelope's inner boundary and the sources of energy considered. We follow de Kool (1990) and express it in terms of a structure parameter λ :

$$E_{\text{bind}} = -\frac{GMM_{\text{env}}}{\lambda R}. \quad (34)$$

By default, COMPAS calculates λ using the ‘‘Nanjing lambda’’ prescription described by Xu & Li (2010a, 2010b), who provide fitting formulae for λ . Our implementation is identical to that of StarTrack (Dominik et al. 2012), including the several improvements they have made to the λ fits. This λ was computed in two different ways; one using only the gravitational binding energy (λ_g) and one that also includes the contribution of the full internal energy²³ (λ_b). COMPAS allows the user to specify a linear combination of the two parameters, $\lambda = \alpha_{\text{th}}\lambda_b + (1 - \alpha_{\text{th}})\lambda_g$. The default is $\alpha_{\text{th}} = 1$, i.e., including the full internal energy.

Alternative COMPAS options to estimate λ include prescriptions for calculating the envelope binding energy from Loveridge et al. (2011), fitting formulae to results from Kruckow et al. (2016) as implemented in Vigna-Gómez et al. (2018), and the option of using a fixed constant value.

We generalize Equations (33) and (34) to include the potential case of a double-core CE (Brown 1995) in the form

$$\begin{aligned} & -\frac{GM_1 M_{1,\text{env}}}{\lambda_1 R_1} - \frac{GM_2 M_{2,\text{env}}}{\lambda_2 R_2} \\ & = \alpha_{\text{CE}} \left(\frac{GM_1 M_2}{2a_{\text{pre-CE}}} - \frac{GM_{1,\text{core}} M_{2,\text{core}}}{2a_{\text{post-CE}}} \right), \end{aligned} \quad (35)$$

where $a_{\text{pre-CE}}$ and $a_{\text{post-CE}}$ are the separation before and after the CE phase, respectively; if one of the $M_{\text{env}} = 0$, then Equation (35) simplifies to the classic single-core energy formalism. Given the simplicity of our parameterization and the short (dynamical) timescales involved in a CE episode, we assume the phase is instantaneous. Equation (35) is used to predict the post-CE orbital separation given the pre-CE binary parameters and the post-CE component masses. The criterion for successful envelope ejection is $a_{\text{post-CE}} > R_1 + R_2$.

After a successful envelope ejection we always assume a circular orbit (see, e.g., Ivanova et al. 2013, for discussion of this). Besides a successful envelope ejection, which leads to a close binary, the CE phase can lead to immediate RLOF or a stellar merger (Section 4.2.5). Immediate RLOF implies that the stripped star or its companion is filling the respective post-CE Roche lobe. By default we allow these systems to engage in a mass transfer episode again, but we flag them so they can be considered as mergers in postprocessing.

A key uncertainty in CE evolution is the fate of Hertzsprung Gap donors (Belczynski et al. 2007). Such stars are not expected to have developed a steep density gradient between core and envelope (Taam & Sandquist 2000; Ivanova & Taam 2004) making it challenging to successfully eject the envelope. It is not clear whether Hertzsprung Gap donor stars can survive CE evolution, or whether instead, this would lead

²³ Note that this includes the thermal energy, radiation energy, ionization energy, and the dissociation energy of molecular hydrogen.

to a merger. In order to account for this uncertainty, we adopt two extreme models following Dominik et al. (2012). In the “optimistic” model, CE events involving a Hertzsprung Gap donor are treated in the same way as a more evolved star, determining the fate of the binary according to the energy budget (Equation (35)). In the “pessimistic” model, it is assumed that all CE events involving a Hertzsprung Gap donor result in a stellar merger. COMPAS keeps track of systems that experience an “optimistic” CE event, allowing the user to remove them in postprocessing. For the results presented in this paper we use the pessimistic model as the default assumption.

CE events initiated by RLOF from main-sequence donors always lead to a stellar merger. CE events with main-sequence accretors are treated as all other CE events by default, but may optionally always lead to stellar mergers.

There is no mass accretion onto the companion during a CE phase in the default COMPAS model. However, different optional CE accretion rate prescriptions exist for the case of NS accretors, including a user-defined fixed value, or following prescriptions from Osłowski et al. (2011) and MacLeod & Ramirez-Ruiz (2015), as described by Chattopadhyay et al. (2020). Mass accretion during a CE phase involving a BH companion has been investigated with COMPAS by van Son et al. (2020), who considered both accretion of a user-defined fixed fraction of the envelope and the Hoyle–Lyttleton (Hoyle & Lyttleton 1939) accretion rate within a CE following prescriptions from MacLeod & Ramirez-Ruiz (2015) based on Chevalier (1993).

4.2.5. Stellar Mergers

In COMPAS, two stars are assumed to merge when $a \leq (R_1 + R_2)$. This can occur following runaway stable mass transfer, if the envelope fails to be ejected during a CE phase, or if the direction of the supernova kick drastically shrinks the orbit. Currently, stellar mergers are flagged and the calculation is stopped, without subsequent evolution of the merger product.

4.2.6. Massive Overcontact Binaries

COMPAS includes prescriptions for CHE stars (Section 3.4), particularly in the context of CHE binaries (Riley et al. 2021). CHE binaries may arise from massive overcontact binaries, in which stars overflow their Roche lobes and share mass during the main sequence (see, e.g., Marchant et al. 2016). We therefore make an exception for them and relax our criteria for RLOF and mergers (see Riley et al. 2021). We consider that CHE stars in massive overcontact binaries can be filling their Roche lobe throughout the main sequence as long as they do not overflow the second (outer) Lagrangian point (Marchant et al. 2016; Riley et al. 2021). In our model, CHE binaries filling the second (outer) Lagrangian point lead to an imminent stellar merger.

4.3. Supernovae (Binary)

In COMPAS, supernovae lead to NS or BH formation²⁴ (the nomenclature is not necessarily associated with their observational signature). Supernovae occur on timescales much shorter than the timescales we resolve in COMPAS; we therefore assume that they are instantaneous events and that they could occur with uniform probability over all orbital phases.

Supernovae affect the orbit of a binary via instantaneous mass loss and natal kicks (Blaauw 1961; Hills 1983; Brandt &

Podsiadlowski 1995; Kalogera 1996; Tauris & Takens 1998; Hurley et al. 2002). We follow Appendix B of Pfahl et al. (2002b) to solve for the response of the orbital elements to a supernova. This prescription accounts for the natal kick, mass ejection, interaction with the companion during the supernova, and modification of the center-of-mass velocity. If the postsupernova eccentricity of the binary exceeds one, we label the binary as gravitationally unbound and cease further calculations (with an option to continue stellar evolution of the noncompact-object companion, if any).

4.4. Gravitational Radiation

Gravitational radiation releases energy and angular momentum from a binary, reducing both the orbital separation and the eccentricity. In COMPAS we only consider gravitational waves (GWs) after DCO formation and follow Peters (1964) to calculate the time to coalescence as

$$\tau_{\text{GW}} = \frac{15}{304} \frac{a_{\text{DCO}}^4 c^5}{G^3 M_1 M_2 M_{\text{tot}}} \kappa(e_{\text{DCO}}), \quad (36)$$

where a_{DCO} and e_{DCO} are the separation and eccentricity of the binary after the second supernova and $\kappa(e_{\text{DCO}})$ is a function of the eccentricity given by

$$\begin{aligned} \kappa(e_{\text{DCO}}) = & \left[\frac{(1 - e_{\text{DCO}}^2)}{e_{\text{DCO}}^{12/19}} \left(1 + \frac{121}{304} e_{\text{DCO}}^2 \right) \right]^{\frac{870}{2299}} \\ & \times \int_0^{e_{\text{DCO}}} \frac{e^{29/19} \left(1 + \frac{121}{304} e^2 \right)^{\frac{1181}{2299}}}{(1 - e^2)^{\frac{3}{2}}} de, \quad (37) \end{aligned}$$

where the integral is calculated as a Riemann sum over 10,000 linearly spaced eccentricity bins. For almost circular ($e < 0.01$) or very eccentric ($e > 0.99$) binaries, we use the approximations as presented following Equation (5.14) in Peters (1964). If τ_{GW} is less than a Hubble time, computed with $H_0 = 67.8 \text{ km s}^{-1} \text{ Mpc}^{-1}$ (Planck Collaboration et al. 2016), we classify the DCO as a merger candidate (but see Section 6.4 to see how we account for cosmological evolution).

4.5. Caveats to Binary Evolution in COMPAS

We currently do not include tidal evolution in COMPAS, although tides are believed to play a non-negligible role in massive binary evolution.

We also do not include magnetic braking evolution in COMPAS. Most massive stars are non-magnetic (Donati & Landstreet 2009). Moreover, unlike for low-mass stars, the magnetic braking assumption of negligible mass loss does not hold for radiatively driven stellar winds. We do not expect magnetic braking to play a significant role in the formation of NS and BH binaries.

COMPAS has not been adequately tested in the context of systems hosting white dwarfs.

5. Evolving a Population

Typically users wish to study particular outcomes of stellar or binary system evolution: BBHs that merge within the age of the universe, DNSs, X-ray binaries, etc. The initial attributes of these systems are usually not known a priori, so a population of

²⁴ With the exception of PISNes as discussed in Section 3.8.4.

systems is evolved with the expectation that some of the systems will evolve into systems of interest.

Each single star or binary system in a COMPAS simulation is described at ZAMS by the initial values of the salient attributes: mass and metallicity for single stars; component star masses, separation, eccentricity, and metallicity for binary systems. Users can specify values to be used for each of the initial attributes, or allow values to be drawn from specified distributions.

5.1. Sampling

The population of objects (stars or binary systems) synthesized by COMPAS is intended to be a representative sample from the full population of stars or binary systems in the universe. Sampling allows us to infer information about the full population based on results from the sampled subset—the sampled collection is used as a proxy for the actual population.

COMPAS provides functionality that allows users to sample the initial attributes of systems outside the COMPAS application and provide those initial attribute values to COMPAS via input grid files (Section 2.7.2). This makes it possible to interface with importance sampling via STROOPWAFEL (Broekgaarden et al. 2019), and in principle, allows for interfaces with other sampling tools such as Dartboard (Andrews et al. 2018) or emulation packages (e.g., Barrett et al. 2017).

COMPAS also includes a basic set of initial condition distributions within the main code. This enables Monte Carlo sampling in which users specify, for each star or binary system to be evolved, fixed values for initial attributes that should not be sampled, and COMPAS will sample the remainder using the distributions described below. Each star or binary system is then evolved to its final state, and the results recorded in output files (see Section 2.8).

Here we briefly describe the basic initial parameter distributions available in the core COMPAS code. For simplicity, we assume that the overall distribution of initial parameters is an outer product over independent parameter distributions, despite evidence to the contrary (Abt et al. 1990; Duchêne & Kraus 2013; Moe & Di Stefano 2017; Klencki et al. 2018).

5.2. Single Star/Primary Mass

The initial mass of a single star, or the primary star (the more massive star at ZAMS) in a binary system, $M_{1,i}$, is, unless specified by the user, determined by the initial mass function (IMF) being used. By default, COMPAS uses the Kroupa (2001) IMF, the distribution function of which is given by

$$p(M_{1,i}) \propto M_{1,i}^{-2.3} \quad (38)$$

above $0.5 M_{\odot}$, and $M_{1,i} \in [5.0, 150.0] M_{\odot}$. Other IMF functions (e.g., Salpeter 1955) are available as configurable options. For simplicity, we assume that the IMF is the same for all metallicities.

5.3. Mass Ratio and Secondary Mass

The mass of the secondary star (less massive at ZAMS), $M_{2,i}$, in a binary system being evolved by COMPAS is, unless specified by the user, determined by the mass ratio

$$q_i \equiv M_{2,i} / M_{1,i}, \quad (39)$$

where $q_i \in [0.01, 1.0]$.

In the default COMPAS model, the mass ratio is drawn from a flat distribution (Sana et al. 2012; Kobulnicky et al. 2014). Other distributions for mass ratio provided in COMPAS as options are the distributions described by Duquennoy & Mayor (1991a) and Sana et al. (2012) (Table S3). A minimum value for $M_{2,i}$ can be specified by the user.

5.4. Metallicity

The metallicity, Z_i , of a single star, or both component stars of a binary system, is, unless otherwise specified by the user, given by $Z_i = Z_{\odot} = 0.0142$ (Asplund et al. 2009).

Users can specify that metallicity be sampled for each single or binary star (for binary stars, both component stars use the same, sampled, value for metallicity), using a log-uniform distribution:

$$p(Z_i) \propto \frac{1}{Z_i}, \quad (40)$$

where $Z_i \in [0.0001, 0.03]$.

5.5. Semimajor Axis

The initial semimajor axis of a binary star, a_i , is, unless specified by the user, sampled independently of the masses using a log-uniform distribution:

$$p(a_i) \propto \frac{1}{a_i}, \quad (41)$$

where $a_i \in [0.01, 1000]$ au (Öpik 1924; Abt 1983).

Other distributions for semimajor axis provided in COMPAS as options are those described by Duquennoy & Mayor (1991b) and Sana et al. (2012). A custom method allows the user to specify parameters of the distribution.

5.6. Orbital Period

The orbital period can be specified for binary stars instead of the semimajor axis. The user can either specify a value for the orbital period, P_i , or that the value be sampled. If the value is sampled, a log-uniform distribution is used:

$$p(P_i) \propto \frac{1}{P_i}, \quad (42)$$

where $P_i \in [1.1, 1000]$ days.

5.7. Orbital Eccentricity

Unless otherwise specified by the user, the COMPAS default model assumes all binary stars are circular at birth (i.e., initial eccentricity $e_i = 0$). Other distributions for eccentricity provided in COMPAS as options are:

1. a flat distribution, $p(e_i) = 1$,
2. a thermal eccentricity distribution $p(e_i) = 2e_i$ (Heggie 1975),
3. the M35 distribution described by Geller et al. (2013),
4. the distribution described by Duquennoy & Mayor (1991a), and
5. the distribution described by Sana et al. (2012, Table S3).

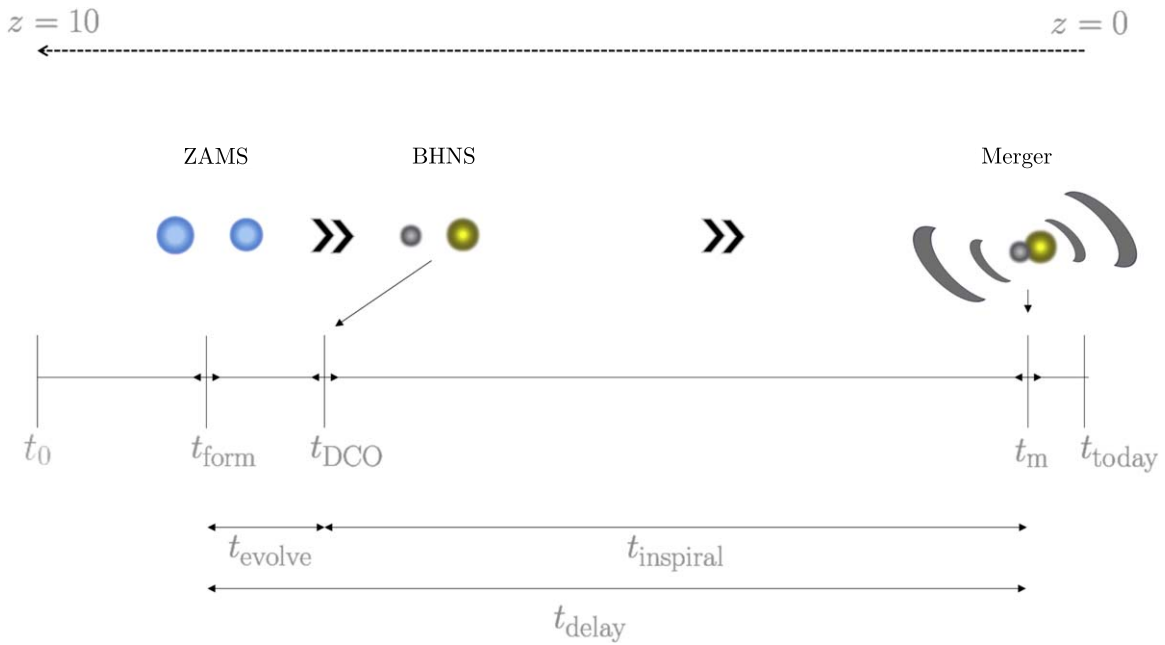


Figure 9. Schematic display of the different times in the formation and evolution of a binary system that impact the time t_m at which a DCO (here a BHNS) system will merge in the history of the universe. The relevant timescales are: the moment the binary is formed at ZAMS from a gas cloud, t_{form} , the moment of DCO formation, t_{DCO} , the time at which the merger takes place, t_m , the time it takes the binary to evolve from ZAMS to the DCO system, $t_{\text{evolve}} = t_{\text{DCO}} - t_{\text{form}}$, the inspiral time, $t_{\text{inspiral}} = t_m - t_{\text{DCO}}$ and the time between binary formation at ZAMS and merger, $t_{\text{delay}} = t_m - t_{\text{form}}$. All mergers that occur within the horizon distance of GW detectors are potentially detectable today. Arrows indicate that those times that vary per binary system. Figure from Broekgaarden et al. (2021a) available at https://github.com/FloorBroekgaarden/BlackHole-NeutronStar/tree/main/plottingCode/Fig_1/variatiions.

5.8. Supernova Kicks

Stars that experience a supernova event may experience a momentum boost as a result of the explosion (see Section 3.7). Unless otherwise specified by the user, the attributes of these so-called natal kicks (i.e., magnitude and direction) are drawn from default distributions, depending upon the supernova type and expected remnant. The COMPAS model for natal kicks is described in detail in Section 3.9.

5.9. Stellar Rotation

Unless otherwise specified by the user, the COMPAS default model assumes that all stars are nonrotating at birth (i.e., the initial rotational velocity $v_{\text{rot}} = 0 \text{ km s}^{-1}$). Other rotation distributions provided in COMPAS as options are:

1. the initial, individual rotational velocities for the two stars can be provided separately,
2. the rotational velocity distribution from Hurley et al. (2000),
3. a rotational velocity distribution for O and B stars based on results from the VLT-FLAMES survey (Ramírez-Agudelo et al. 2013).

We describe the limited aspects of rotation currently modeled by COMPAS in Section 3.4. For stars in binaries, if CHE is enabled (default), COMPAS overwrites the drawn or zero rotational velocities of the binary components with the orbital velocity of the binary (i.e., tidal locking is assumed).

6. Postprocessing

Using binary population synthesis simulations to make predictions and calculations for astrophysical populations requires converting the data from the simulation into meaningful astrophysical quantities. The foremost example, for

compact objects, is calculating DCO formation and merger rates as a function of redshift and/or component masses. The strengths of the COMPAS suite include its publicly available postprocessing scripts where these calculations are performed. This section describes the methodology behind the main postprocessing scripts that are publicly available in COMPAS.²⁵

6.1. Recording Properties

As described in Section 2.8, during the simulation, COMPAS calculates and records properties of the stars and/or binary systems such as the ages, masses, stellar radii, effective temperatures, velocities, eccentricities, and separations. The user can specify which properties are recorded and when during the simulation they are reported. Examples include the option to save the properties at every time step (*detailed output*, an example is given in Section 7.1) or only printing the properties of the binary at important evolutionary stages of the binary such as CE episodes and SNe. A detailed description of how the output can be specified is given in the code documentation.²⁰

6.2. Selecting Binary Systems of Interest

During a simulation, COMPAS returns the recorded properties of all of the simulated binary systems. Further subselection of binaries of specific interest, such as BBHs that merge in a Hubble time or systems that experienced a CE event, is done by means of postprocessing. The “optimistic” and “pessimistic” CE selection (as mentioned in Section 4.2.4) is also performed in postprocessing. The subselection of systems of interest is typically done in COMPAS by “slicing” or “masking” the data, which is described in the publicly available jupyter notebooks.

²⁵ <https://github.com/TeamCOMPAS/COMPAS>

6.3. Converting to Yields per Star-forming Mass

A COMPAS simulation is typically performed by modeling only a fraction of the underlying stellar population by, for example, not simulating single stars and/or not drawing the simulated binaries from their full initial birth distributions (e.g., by only simulating stars with masses $\geq 5 M_{\odot}$). To obtain meaningful estimates for formation rates of the binaries of interest, the population synthesis simulation is typically re-normalized to a formation yield per unit star-forming mass. In this section we will often write this DCO formation yield as a function of: birth metallicity Z_i ,²⁶ delay time t_{delay} (i.e., the time between the formation and the merger of a binary, see Figure 9), and compact object masses M_1 , M_2 . Doing so, the DCO formation yield for a binary with metallicity Z_i , delay time t_{delay} and final compact object masses M_1 and M_2 can be written as

$$\frac{d^4 N_{\text{form}}}{dM_{\text{SFR}} dt_{\text{delay}} dM_1 dM_2}(Z_i, t_{\text{delay}}, M_1, M_2),$$

where N_{form} is the number of systems of interest that form and M_{SFR} is a unit of star-forming mass. To get the total yield $dN_{\text{form}}/dM_{\text{SFR}}$ this is marginalized over t_{delay} , M_1 and M_2 . This yield is typically computed with a Monte Carlo approach through COMPAS simulations. The subsequent conversion to merger and detection rates is then done in postprocessing, as described below.

6.4. Calculating Astrophysical Rates over the Cosmic History of Our Universe: The Case of Double Compact Object Mergers

These COMPAS suite scripts to calculate cosmological formation and merger rates of astrophysical events, often referred to as ‘‘cosmological integration,’’ are based on the work presented in Neijssel et al. (2019). We describe the method behind these postprocessing scripts for the example of calculating DCO merger rates over redshift below, similarly to Neijssel et al. (2019) and Broekgaarden et al. (2021a), but the idea can be easily generalized to other phenomena.

6.4.1. Double Compact Object Merger Rates for Ground-based GW Detectors

The DCO merger rate measured by a comoving observer in the source frame of the merger at a given merger time t_m (measured since the Big Bang) is given by

$$\begin{aligned} \mathcal{R}_m(t_m, M_1, M_2) &\equiv \frac{d^4 N_{\text{merger}}}{dt_m dV_c dM_1 dM_2}(t_m, M_1, M_2) \\ &= \int dZ_i \int_0^{t_m} dt_{\text{delay}} \text{SFRD}(Z_i, z(t_{\text{form}} = t_m - t_{\text{delay}})) \\ &\quad \times \frac{d^4 N_{\text{form}}}{dM_{\text{SFR}} dt_{\text{delay}} dM_1 dM_2}(Z_i, t_{\text{delay}}, M_1, M_2), \end{aligned} \quad (43)$$

where we convolve the yield with the the metallicity-specific star formation rate density $\text{SFRD}(Z_i, z(t_{\text{form}}))$, which is a function of birth metallicity Z_i and redshift z .²⁷ In Equation (43) V_c is the comoving volume and the relevant star formation rate is computed at a redshift corresponding to the formation time

$t_{\text{form}} = t_m - t_{\text{delay}}$. Delay times and metallicities are integrated over. We describe the merger rate in Equation (43) as an explicit function of M_1 and M_2 because the probability of a DCO merger detection depends on their values (see below), but the total merger rate is often computed by marginalizing over the DCO component masses.

We obtain the SFRD (Z_i, z) by multiplying the total star formation rate density (SFRD) with a metallicity probability density function

$$\begin{aligned} \text{SFRD}(Z_i, z_{\text{form}}) &\equiv \frac{d^3 M_{\text{SFR}}}{dt_s dV_c dZ_i}(z_{\text{form}}) \\ &= \underbrace{\frac{d^2 M_{\text{SFR}}}{dt_s dV_c}(z_{\text{form}})}_{\text{SFRD}} \times \underbrace{\frac{dP}{dZ_i}(z_{\text{form}})}_{\text{GSMF+MZR}}, \end{aligned} \quad (44)$$

where we used the short hand notation $z_{\text{form}} = z(t_{\text{form}})$. In the available COMPAS postprocessing scripts, the metallicity distribution function, dP/dZ_i , is typically described as a convolution between a galaxy mass function, the number density of galaxies per logarithmic mass bin (GSMF) and the mass–metallicity relation (MZR). This is discussed in more detail in the following sections and schematically shown in Figure 10.

In practice, the integral in Equation (43) is approximated by a Monte Carlo estimate, integrating over simulated metallicities. The metallicities in the integral limit in Equation (43) that fall outside of the simulated metallicity range can be either included in the edge bins (see, e.g., Broekgaarden et al. (2021a) for more details) or conservatively ignored (effectively curtailing dP/dZ_i to zero outside the range of simulated metallicities).

The DCO merger rate in Equation (43) is then converted to a local detection rate \mathcal{R}_{det} by integrating over the comoving volume and taking into account the probability P_{det} of detecting a gravitational-wave source (Section 6.6) using

$$\begin{aligned} \mathcal{R}_{\text{det}}(t_{\text{det}}, M_1, M_2) &\equiv \frac{d^3 N_{\text{det}}}{dt_{\text{det}} dM_1 dM_2} \\ &= \int dz \frac{dV_c}{dz} \frac{dt_m}{dt_{\text{det}}} \mathcal{R}_m(t_m) P_{\text{det}}(M_1, M_2, z(t_m)), \end{aligned} \quad (45)$$

where t_{det} is the time in the detector (i.e., the observer) frame, $P_{\text{det}}(M_1, M_2, z)$ is the probability of detecting a gravitational-wave signal from a binary with component masses M_1 , M_2 merging at redshift z , and $\frac{dt_m}{dt_{\text{det}}} = \frac{1}{(1+z)}$ and $\frac{dV_c}{dz}$ are given by, e.g., Hogg (1999). In practice, this integral over redshift can be computed as a Riemann sum over discrete redshift bins; see, e.g., previous work by Dominik et al. (2013, 2015), Belczynski et al. (2016b), Mandel & de Mink (2016), Eldridge et al. (2019b), Baibhav et al. (2019), Bavera et al. (2020), Chruslinska et al. (2019). The total detection rate per unit time can be obtained by further integrating over DCO masses.

6.5. Metallicity-specific Star Formation Rate Density Prescriptions

In COMPAS, the current publicly available postprocessing scripts use convolutions between analytical prescriptions for the SFRD, GSMF, and MZR (Equation (44)). The analytical equations are based on observations and simulations and can be flexibly adapted to the user’s preferences. We present below

²⁶ Before we used Z instead of Z_i for metallicity. In the remaining section we use Z_i to be consistent with the notation for other birth parameters.

²⁷ We use SFRD for the star formation rate density, and $\text{SFRD}(Z_i, z)$ for the metallicity-specific star formation rate density.

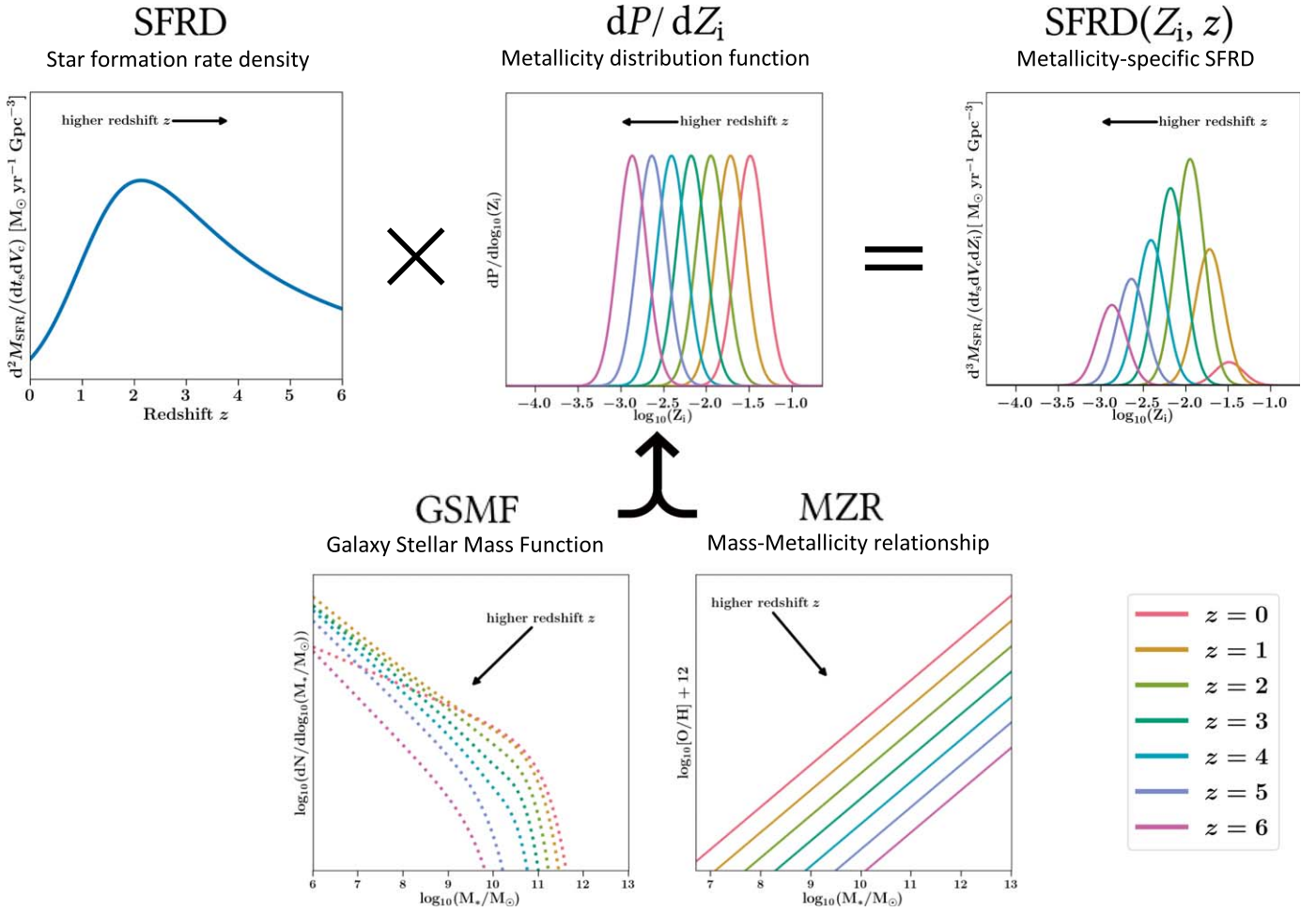


Figure 10. Schematic depiction of how models for the metallicity-specific star formation rate density, SFRD (Z_i, z), can be created in COMPAS by multiplying a star formation rate density with a metallicity probability distribution function, dP/dZ_i . The metallicity distribution function is typically constructed in the available COMPAS postprocessing scripts by convolving a galaxy stellar mass function with a mass–metallicity relationship. An exception is the “preferred” model from Neijssel et al. (2019), which uses a phenomenological model directly for the metallicity distribution function. The arrows in each subfigure indicate in which direction the distribution moves as redshift increases. Original figure from Broekgaarden et al. (2021a) available at https://github.com/FloorBroekgaarden/BlackHole-NeutronStar/tree/main/plottingCode/fig_2.

the prescriptions existing in COMPAS postprocessing based on the work from Neijssel et al. (2019). An overview of the default available options for those prescriptions is given in Table 3.

6.5.1. Star Formation Rate Density Prescriptions

The COMPAS cosmic integration postprocessing scripts have different options for the SFRD. Several examples are given in the second column of Table 3 and shown in Figure 11. One of the SFRD prescriptions is based on the “preferred” model from Neijssel et al. (2019), which is calibrated to match the GW detections from the first two observing runs of LIGO and Virgo. Two other options are the Madau & Dickinson (2014) and Madau & Fragos (2017) SFRDs. All three SFRDs are given by the functional form

$$\frac{d^2 M_{\text{SFR}}}{dt_s dV_c}(z) = b_1 \frac{(1+z)^{b_2}}{1 + [(1+z)/b_3]^{b_4}} M_{\odot} \text{ yr}^{-1} \text{ Mpc}^{-3}. \quad (46)$$

where z is the redshift. The parameters b_1 , b_2 , b_3 , and b_4 in the equation for the SFRD are defined by: $b_1 = 0.01$, $b_2 = 2.77$, $b_3 = 2.9$ and $b_4 = 4.7$ for the preferred model in Neijssel et al. (2019); $b_1 = 0.015$, $b_2 = 2.7$, $b_3 = 2.9$ and $b_4 = 5.6$ for the Madau & Dickinson (2014) prescription (see their Equation

(15)) and $b_1 = 0.01$, $b_2 = 2.6$, $b_3 = 3.2$ and $b_4 = 6.2$ for the Madau & Fragos (2017) prescription (see their Equation (1)). Another available SFRD is the one from Strolger et al. (2004, see their Equation (1)), which uses an extinction-corrected model for SFRD described as a function of the universe’s age:

$$\begin{aligned} & \frac{d^2 M_{\text{SFR}}}{dt_s dV_c}(t_{\text{form}}) \\ &= c_1 \left[t_{\text{form}}^{c_2} \exp\left(-\frac{t_{\text{form}}}{c_3}\right) + c_4 \exp\left(c_4 \frac{t_{\text{form}} - t_0}{c_3}\right) \right] \frac{M_{\odot}}{\text{yr Mpc}^3}, \end{aligned} \quad (47)$$

with $c_1 = 0.182$, $c_2 = 1.26$, $c_3 = 1.865$, $c_4 = 0.071$, and $t_0 = 13.47$ Gyr.

6.5.2. Metallicity Distribution Function over Redshift (GSMF + MZR)

The chemical evolution of star formation in our universe is described in the COMPAS postprocessing scripts by the metallicity probability density, dP/dZ_i , which is a function of redshift. The cosmic integration postprocessing scripts offer several options for the metallicity density function, several examples are shown in Figure 12.

Table 3

Examples of the By-default Available Options to Construct a Metallicity-specific Star Formation Density Model SFRD(Z_i, z) in the Publicly Available Cosmic Integration Postprocessing Scripts of COMPAS

xyz index	SFRD [x]	GSMF [y]	MZR [z]
0 (default)	“Preferred” phenomenological model from Neijssel et al. (2019)		
1	Madau & Dickinson (2014)	Panter et al. (2004)	Langer & Norman (2006)
2	Stolger et al. (2004)	Furlong et al. (2015) single Schechter	Langer & Norman (2006) + offset
3	Madau & Fragos (2017)	Furlong et al. (2015) double Schechter	Ma et al. (2016a)

Note. A SFRD (Z_i, z) model can be obtained by combining a star formation rate (SFR) with a galaxy stellar mass function (GSMF) and mass–metallicity relation (MZR). See Sections 6.4 for more details. The labels 0, 1, 2, 3 are solely used in the figures to refer to these models. The code is flexible to easily adopt a user-specified prescription for the SFRD, GSMF, or MZR.

The preferred model from Neijssel et al. (2019) ($yz = 00$ in Table 3) uses a phenomenological model, which defines the metallicity density function as a symmetric log-normal distribution:

$$\frac{dP}{dZ_i}(z) = \frac{1}{Z_i \sigma_1 \sqrt{2\pi}} \exp\left(-\frac{(\ln(Z_i) - \mu_1(z))^2}{2\sigma_1^2}\right), \quad (48)$$

where σ_1 is the standard deviation in $\ln(Z)$ -space and $\mu_1(z)$ is the redshift-dependent mean in $\ln(Z)$ -space. Neijssel et al. (2019) use a redshift independent $\sigma_1 = 0.39$ and mean $\mu_1 = \langle \ln(Z) \rangle$ defined by

$$\langle Z(z) \rangle = \exp(\mu_1 + \sigma_1^2/2) = Z_0 10^{e_1 z}, \quad (49)$$

where Z_0 is the mean metallicity at redshift 0. In the preferred phenomenological model, $Z_0 = 0.035$ and $e_1 = -0.23$.

This parameterization of the mean (Equation (49)) follows the work by Langer & Norman (2006). Observational evidence suggests the metallicity distributions are likely not symmetric in log-metallicity (e.g., Langer & Norman 2006; Chruslinska et al. 2019; Boco et al. 2021). The other prescriptions for the metallicity distribution function, which are available in the COMPAS postprocessing, are therefore asymmetric convolutions of a GSMF and an MZR.

6.5.3. Galaxy Stellar-mass Function Prescriptions

The available GSMFs in the COMPAS postprocessing scripts are all based on observations of luminosity distributions of galaxies, which are converted to galaxy mass distributions based on a luminosity–mass relation. The options are listed in the third column of Table 3 and in Figure 13. More details are provided in Appendix A3 of Neijssel et al. (2019).

The GSMFs 1 and 2 use a functional form of a single Schechter function given by

$$\Phi_{M_*}(z) dM_* = \phi_1(z) \left(\frac{M_*}{M_c(z)}\right)^{-\psi_1(z)} \exp\left(\frac{-M_*}{M_c(z)}\right) dM_*, \quad (50)$$

where M_* is the galaxy stellar mass, ϕ_1 is the overall normalization, ψ_1 is the parameter for the slope of the GSMF for $M_* \leq M_c$ and M_c is the cutoff where the GSMF moves from a power-law into an exponential drop off (see Figure 13). Panter et al. (2004, Equation (1)) use a z -independent single Schechter function with $\phi_1 = 7.8 \times 10^{-3} \text{ Mpc}^{-3}$, $\psi_1 = +1.16$ and $M_c = 7.64 \times 10^{10} M_\odot$. The GSMF option “Furlong et al. (2015) single” ($y = 2$ in Table 3), uses a linear fit by Neijssel et al. (2019) to the tabulated redshift-dependent values for ϕ_1 , ψ_1 , and M_c . The GSMF option “Furlong et al. (2015) double”

($y = 3$ in Table 3) is instead based on a double Schechter function given by

$$\Phi_{M_*}(z) dM_* = \exp\left(\frac{-M_*}{M_c(z)}\right) \times \left[\phi_1(z) \left(\frac{M_*}{M_c(z)}\right)^{-\psi_1(z)} + \phi_2(z) \left(\frac{M_*}{M_c(z)}\right)^{-\psi_2(z)} \right] dM_*, \quad (51)$$

which is fitted in a similar way based on tabulated data.

6.5.4. Mass–Metallicity Relation Prescriptions

The default MZR in the COMPAS postprocessing scripts are analytical formulas for the mapping between galaxy stellar mass and the metallicity of star formation. Outside of the phenomenological model by Neijssel et al. (2019), there are three different MZR available by default in COMPAS.

The MZR 1 and 2 in Table 3 are based on Langer & Norman (2006), who derive a MZR based on Savaglio et al. (2005) observations of 56 galaxies in the Gemini Deep Deep and Canada–France Redshift Survey. They obtain a bisector fit, which is then simplified by Langer & Norman (2006) resulting in the MZR

$$\frac{M}{M_*} = \left(\frac{Z_i}{Z_\odot}\right)^2, \quad (52)$$

with $M_* = 7.64 \times 10^{10} M_\odot$ from Panter et al. (2004), and a mean metallicity that scales with redshift as Equation (49) with the COMPAS default values of $Z_0 = 0.035$, $\alpha = 0.3$. Combining these two relations results in the MZR by Langer & Norman (2006) given in Table 3 with the label $z = 1$. However, since this MZR has an offset from the Savaglio et al. (2005) bisector fit, Neijssel et al. (2019) also added a second default MZR prescription based on Langer & Norman (2006) with a fixed offset in metallicity to match the results by Savaglio et al. (2005).

The MZR from Ma et al. (2016a) is based on theoretical models of cosmological simulations combined with population synthesis simulations. Their MZR is given by

$$\begin{aligned} & \log_{10}(Z_{\text{gas}}/Z_\odot) \\ &= 0.35 \left[\log_{10}\left(\frac{M_*}{M_\odot}\right) - 10 \right] + 0.93 \exp(-0.43z) - 1.05, \end{aligned} \quad (53)$$

with Z_{gas} the metallicity of the star-forming gas (here Z_i).

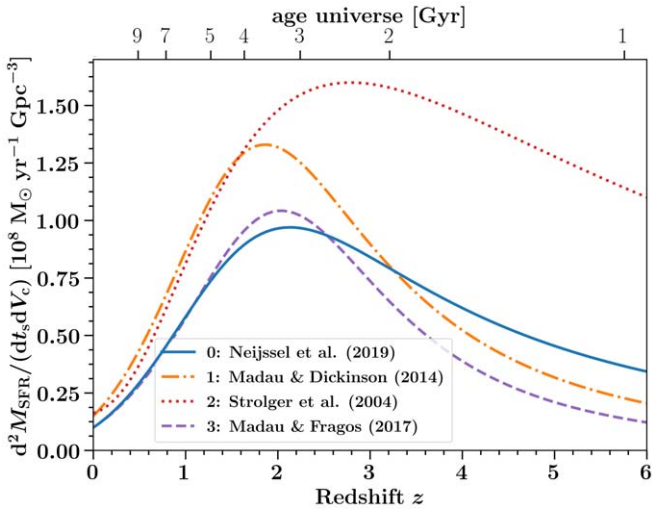


Figure 11. The star formation rate density as a function of redshift for the four default available options in the cosmic integration postprocessing scripts of COMPAS.

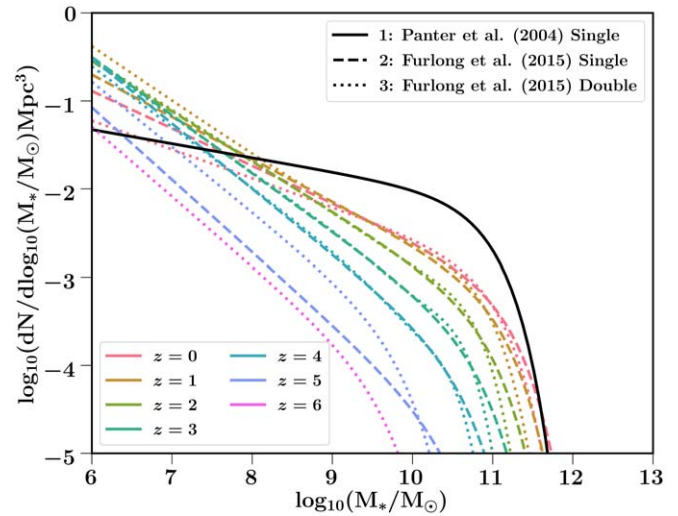


Figure 13. The galaxy stellar mass functions (GSMFs) for the three default available options in the cosmic integration postprocessing scripts of COMPAS (see also Table 3). The GSMFs are shown at seven different redshift values, except for the Panter et al. GSMF, which is not redshift-dependent.

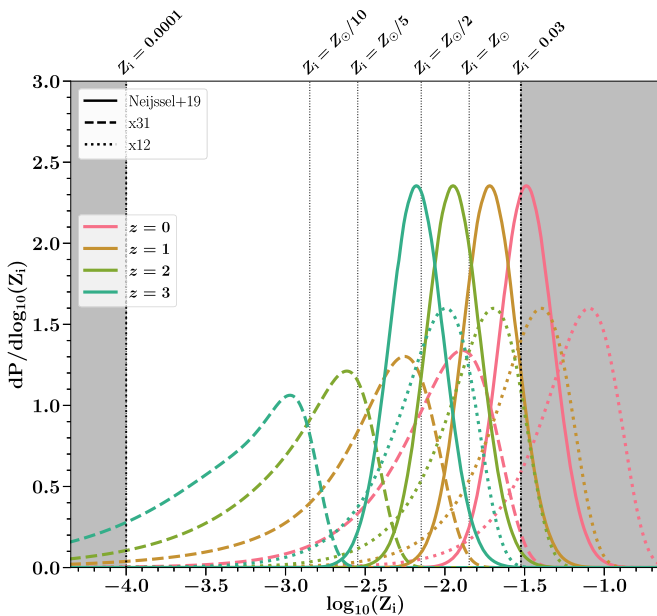


Figure 12. Three examples of metallicity probability distribution functions (dP/dZ_i) available in the postprocessing scripts of COMPAS. For each of the prescriptions the metallicity distribution is shown for four different redshifts. Gray areas show Z_i values that fall outside of the metallicity range of SSE tracks from Hurley et al. (2000).

The three MZR options available by default in COMPAS are given in Figure 14.

6.6. Gravitational-wave Selection Effects

Whether a DCO merger is detectable by a GW interferometer depends on its distance (i.e., redshift), orientation, inclination, and source component masses M_1 and M_2 . The detectability by a network is approximated by checking whether the source signal-to-noise ratio (S/N) in a single detector surpasses a predefined threshold. COMPAS contains

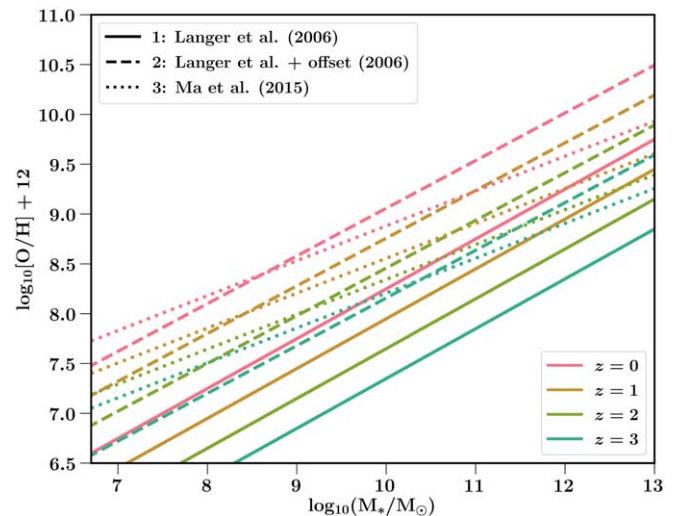


Figure 14. The mass-metallicity relations for the three default available options in the cosmic integration postprocessing scripts of COMPAS. The MZR are shown at different redshift values.

publicly available postprocessing scripts that calculate the detection probability of a gravitational-wave source, based on the method described in Barrett et al. (2018). Source component spins and any residual in-band eccentricity are not currently included in these detection probability estimates.

Typically a user sets in the COMPAS postprocessing scripts a S/N threshold of $S/N = 8$ for a single ground-based GW detector (Finn & Chernoff 1993), such that sources with a higher S/N are detectable, but this can be changed to the user-specified value. The S/Ns of the DCO mergers are calculated by computing the source waveforms using a user-chosen waveform model included in the LAL software suite (LIGO Scientific Collaboration 2018), such as IMRPHENOMPV2 (Hannam et al. 2014; Husa et al. 2016; Khan et al. 2016) and SEOBNRV3 (Pan et al. 2014; Babak et al. 2017). We marginalize over the sky localization and source orientation

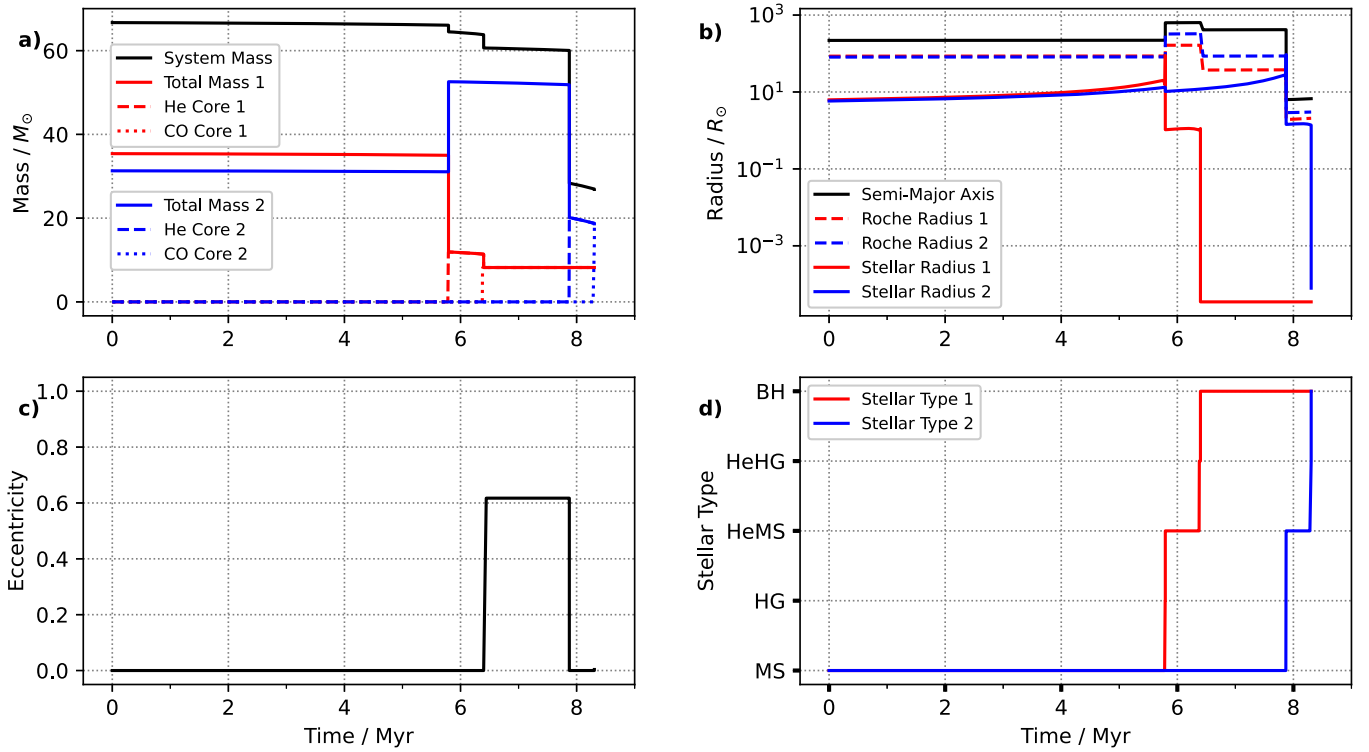


Figure 15. Plots produced using detailed COMPAS output of the evolution of a with initial masses $M_{\text{ZAMS},1} = 35.4 M_{\odot}$, $M_{\text{ZAMS},2} = 29.3 M_{\odot}$ on a circular orbit with semimajor axis $a = 1.02\text{AU}$ at metallicity $Z = 0.001$. These initial parameters produce a GW151226-like BBH with component masses 15.9 and $8.2 M_{\odot}$ and a coalescence time of 280 Myr (GW151226 had measured component masses of $14.2^{+8.3}_{-3.7}$ and $7.5^{+2.3}_{-2.3} M_{\odot}$, Abbott et al. 2016b). Panels (a)–(d) plot respectively the time evolution of the mass parameters (masses of both stars and their He and CO cores, and the total mass of the binary), the radius parameters (stellar radii and Roche radii for both stars, and the semimajor axis), eccentricity, and stellar types (as described in Table 2). Red, blue, and black lines denote the primary star, secondary star, and the binary, respectively.)

of the binary using the antenna pattern function from Finn & Chernoff (1993). The detector sensitivity can be chosen by the user. Available options include the sensitivity of a LIGO instrument at design sensitivity and O1, O2, and O3 configurations (Aasi et al. 2015; Abbott et al. 2016a), as well as the third-generation Einstein Telescope detector (Hild et al. 2011).

7. Usage Examples

In this section, we show a few practical examples of COMPAS usage. Although COMPAS has mainly been applied to large population studies (see examples in Section 1), it is often useful to visualize the full evolutionary path of a given isolated binary, especially when trying to reproduce a specific system. We show an example in Section 7.1, with the caveat that the approximate treatment of rapid population synthesis cannot match the precision of detailed stellar codes for individual systems. In Section 7.2 we show a more typical application of COMPAS postprocessing tools to predict a distribution over a population, in this case, the chirp mass distribution of detectable BBH mergers.

7.1. Detailed Evolution of a Binary

We provide an example plot of the COMPAS detailed output in Figure 15, which records the detailed evolution of the progenitor to a GW151226-like BBH (Abbott et al. 2016b; Stevenson et al. 2017). The code to reproduce this binary and the detailed output of any binary is available at <https://github.com/TeamCOMPAS/COMPAS>.

We now describe the evolution of this example binary system. Descriptions of the stellar types referenced below can be found in Table 2.

- Figure 15(b) shows that the primary star (red line) exceeds its Roche lobe at 5.8 Myr and initiates mass transfer as it expands rapidly once it evolves off the main sequence. This dynamically stable mass transfer episode is nonconservative, as reflected by the concurrent dip in total mass (black curve in Figure 15(a)). This causes the semimajor axis to nearly triple, despite the larger initial mass of the donor (see Equation (25)). Figure 15(a) shows that the primary loses $23 M_{\odot}$ (corresponding to its hydrogen envelope), of which $21 M_{\odot}$ is accreted by the secondary. The primary emerges as a stripped Helium star (HeMS), as shown in Figure 15(d), with total mass equal to its He-core mass (Figure 15(a)).
- After another 0.6 Myr, the primary collapses into a BH in a core-collapse supernovae (CCSNe), ejecting $3 M_{\odot}$ in the process (Figure 15(a)). Its natal kick induces an orbital eccentricity of 0.62 (Figure 15(c)), but due to a fortuitous combination of kick magnitude and direction, the orbital semimajor axis shrinks by $\sim 1/3$ (Figure 15(b)).
- The secondary evolves off the main sequence at 7.8 Myr (Figure 15(d)). It too expands and exceeds its Roche lobe shortly thereafter, triggering dynamically unstable mass transfer back onto the primary (now a BH, Figure 15(b)). The binary enters a CE, characterized by orbital tightening by several orders of magnitude (Figure 15(b)) on the dynamical timescale of the donor. In the default COMPAS

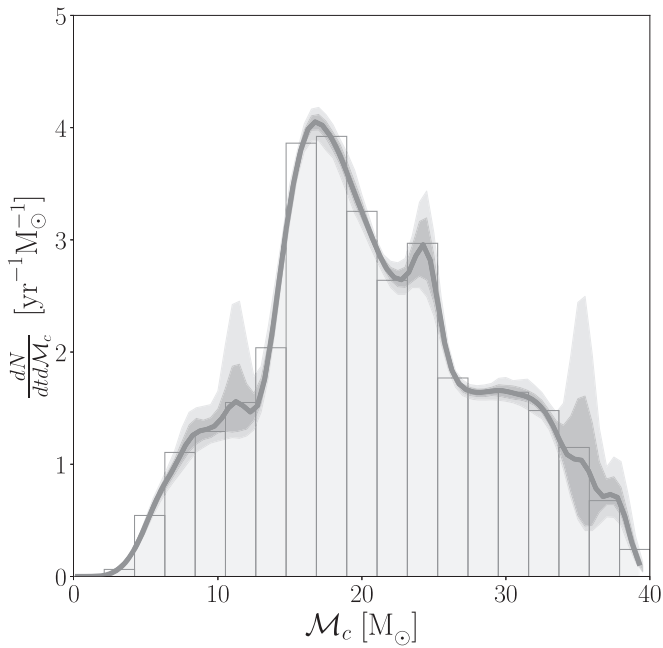


Figure 16. Distribution of the detection rate of BBH mergers over chirp mass, assuming LIGO O3 sensitivity, an S/N threshold of 8, and the default metallicity-specific star formation history model from Neijssel et al. (2019). The gray bars show a binned histogram. The thick gray smooth solid line is a kernel density estimate of the distribution, and the shaded region shows the one and two σ sampling uncertainties estimated through bootstrapping.

model, CE phases are assumed to completely circularise the binary, removing the eccentricity imparted by the first SNe (Figure 15(c)).

4. The secondary is stripped by the CE episode and continues its evolution as a stripped helium star (HeMS) (Figure 15(d)), collapsing into a BH at 8.3 Myr. The complete fallback in the second supernova results in no natal kick and a consequently small post-SNe eccentricity (Figure 15(c)).

7.2. Chirp Mass Distribution of LIGO BBHs

We show an example application of COMPAS population postprocessing tools to predict the chirp mass distribution of BBHs detected by gravitational-wave detectors.

We evolve ten million binaries with COMPAS assuming the default model. Metallicities are sampled log-uniformly in the range $\log(Z) \in [0.0001, 0.03]$. A Monte Carlo integral over a smooth distribution of metallicities (see Section 6.4) avoids the metallicity binning artefacts encountered when using a discrete metallicity grid, as discussed, e.g., by Dominik et al. (2015). We compute the merger rate distribution under the assumption of a phenomenological, metallicity-specific star formation history (see Section 6.5) detailed in Neijssel et al. 2019. We apply gravitational-wave selection effects (see Section 6.6) for a LIGO detector network operating at O3 sensitivity and a S/N detection threshold of 8. Figure 16 shows the chirp mass distribution of detectable BBHs.

The script used to make this plot, which makes use of COMPAS’s postprocessing classes, can be found at <https://github.com/TeamCOMPAS/COMPAS>.

8. Conclusions

We described COMPAS, a public rapid binary population synthesis code. COMPAS v 02.21.00 evolves ~ 100 binaries per second on a modern laptop computer. Given its parallel structure (jobs can be readily split across multiple cores with no need for communication until results are re-combined), a population of a billion binaries can be evolved in 24 hours on a modest 128 core cluster. COMPAS is designed to make it easy to specify desired parameterized prescriptions or introduce new models for various stages of stellar and binary evolution. Together with its postprocessing toolbox, COMPAS is thus well suited for inference studies on observed stellar binary populations (e.g., Barrett et al. 2018).

The following are some of the planned enhancements to COMPAS that we hope to include in future versions:

1. COMPAS currently relies on Hurley et al. (2000) models for single stellar evolution. In order to evaluate the impact of uncertainties in these models, we plan to incorporate single stellar evolution tracks interpolated from other stellar evolution codes with METISSE (Method of Interpolation for Single Star Evolution, Agrawal et al. 2020).
2. Extend COMPAS to more accurately treat low-mass stars. While the code can evolve binaries with low-mass components, a number of features, ranging from white dwarf novae to magnetic braking, are either not included or insufficiently tested.
3. Include a proper treatment of stellar mergers, allowing the future evolution of merger products to be tracked.
4. Update and re-activate the treatment of tidal interactions, including tidal synchronization and circularization, to include the latest models (e.g., Vick & Lai 2020).

COMPAS is a public code, and we encourage the community to use it and, should they wish, to become involved in its development. In particular, any defects or enhancement requests can be brought to our attention via the github issue tracker²⁸ or by e-mail, compas-user@googlegroups.com. COMPAS will be published in the *Journal of Open Source Software* (Team Compas et al. 2021).

The authors thank Ben Bradnick, Isobel Romero-Shaw, and Rajath Sathyaprakash for past contributions to the code, and Simone Bavera, Chris Belczynski, Christopher Berry, Jan Eldridge, Tassos Fragos, David Hendriks, Jarrod Hurley, Vicky Kalogera, Morgan MacLeod, Pablo Marchant, Javier Morán Fraile, Philipp Podsiadlowski, Carl Rodriguez, Dorottya Szécsi, and Michael Zevin for discussions and advice. Multiple authors are supported by the Australian Research Council Centre of Excellence for Gravitational Wave Discovery (OzGrav), through project No. CE170100004. Multiple authors were funded in part by the National Science Foundation under grant No. (NSF grant No. 2009131), the Netherlands Organization for Scientific Research (NWO) as part of the Vidi research program BinWaves with project No. 639.042.728 and by the European Union’s Horizon 2020 research and innovation program from the European Research Council (ERC, grant agreement No. 715063). F.S.B. is supported in part by the Prins Bernard Cultuurfonds studiebeurs. I.M. is a recipient of an Australian Research Council Future Fellowship

²⁸ <https://github.com/TeamCOMPAS/COMPAS/issues>

(FT190100574). A.V.G. acknowledges funding support by the Danish National Research Foundation (DNRF132).

This research has made use of NASA's Astrophysics Data System Bibliographic Services.²⁹

Facilities: Some of the results in this manuscript were obtained using the following computing facilities: FAS Research Computing, Harvard University, and the OzSTAR national facility at Swinburne University of Technology. The OzSTAR program receives funding in part from the Astronomy National Collaborative Research Infrastructure Strategy (NCRIS) allocation provided by the Australian Government.

Software: COMPAS is written in C++ and we acknowledge the use of the GNU C++ compiler, GNU scientific library (gsl), the BOOST C++ library, and the HDF5 C++ library from <http://www.gnu.org/software/gsl/> (Galassi et al. 2002). The COMPAS suite makes use of Python from the Python Software Foundation. Python Language Reference available at <http://www.python.org> (van Rossum 1995). In addition, the COMPAS suite makes use of the python packages Astropy³⁰ (Astropy Collaboration et al. 2013, 2018), hdf5³¹ (Collette 2013), the IPython,³² and Jupyter notebook package³³ (Pérez & Granger 2007; Kluyver et al. 2016), Matplotlib³⁴ (Hunter 2007), NumPy³⁵ (Harris et al. 2020), SciPy³⁶ (Virtanen et al. 2020), Seaborn (Waskom et al. 2020). The COMPAS postprocessing code for detection probability currently makes use of precomputed results from the LALSuite toolkit (LIGO Scientific Collaboration 2018), such as the IMRPHEMOPV2 waveform (Hannam et al. 2014; Husa et al. 2016; Khan et al. 2016).

Data Availability

We encourage the community to make results obtained with COMPAS publicly available at <https://zenodo.org/communities/compas/>. The scripts to reproduce the data and plots for all figures in this manuscript using v02.21.00 of COMPAS are provided in the corresponding directories at <https://github.com/Team-COMPAS/COMPAS>.

ORCID iDs

Jeff Riley  <https://orcid.org/0000-0003-1530-2557>
 Poojan Agrawal  <https://orcid.org/0000-0002-1135-984X>
 Jim W. Barrett  <https://orcid.org/0000-0002-0151-0753>
 Kristan N. K. Boyett  <https://orcid.org/0000-0003-4109-304X>
 Floor S. Broekgaarden  <https://orcid.org/0000-0002-4421-4962>
 Debatri Chattopadhyay  <https://orcid.org/0000-0001-5867-5033>
 Fabian Gittins  <https://orcid.org/0000-0002-9439-7701>
 Ryosuke Hirai  <https://orcid.org/0000-0002-8032-8174>
 George Howitt  <https://orcid.org/0000-0002-2593-0189>
 Stephen Justham  <https://orcid.org/0000-0001-7969-1569>
 Floris Kummer  <https://orcid.org/0000-0002-6056-3070>
 Mike Y. M. Lau  <https://orcid.org/0000-0002-6592-2036>

²⁹ <http://adsabs.harvard.edu/>

³⁰ <http://www.astropy.org>

³¹ <https://docs.h5py.org/en/stable/>

³² <http://ipython.org>

³³ <https://jupyter.org/>

³⁴ <http://www.matplotlib.org>

³⁵ <http://www.NumPy.org/>

³⁶ <https://www.scipy.org>

Ilya Mandel  <https://orcid.org/0000-0002-6134-8946>
 Selma E. de Mink  <https://orcid.org/0000-0001-9336-2825>
 Coenraad Neijssel  <https://orcid.org/0000-0001-9318-5259>
 Lieke van Son  <https://orcid.org/0000-0001-5484-4987>
 Simon Stevenson  <https://orcid.org/0000-0002-6100-537X>
 Alejandro Vigna-Gómez  <https://orcid.org/0000-0003-1817-3586>
 Serena Vinciguerra  <https://orcid.org/0000-0003-3068-6974>
 Tom Wagg  <https://orcid.org/0000-0001-6147-5761>
 Reinhold Willcox  <https://orcid.org/0000-0003-0674-9453>

References

- Aasi, J., Abbott, B. P., Abbott, R., et al. 2015, *CQGra*, **32**, 074001
 Abbott, B. P., Abbott, R., Abbott, T. D., et al. 2016a, *LRR*, **19**, 1
 Abbott, B. P., Abbott, R., Abbott, T. D., et al. 2016b, *PhRvL*, **116**, 241103
 Abbott, B. P., Abbott, R., Abbott, T. D., et al. 2019, *PhRvX*, **9**, 031040
 Abt, H. A. 1983, *ARA&A*, **21**, 343
 Abt, H. A., Gomez, A. E., & Levy, S. G. 1990, *ApJS*, **74**, 551
 Agrawal, P., Hurley, J., Stevenson, S., Szécsi, D., & Flynn, C. 2020, *MNRAS*, **497**, 4549
 Akmal, A., Pandharipande, V., & Ravenhall, D. 1998, *PhRvC*, **58**, 1804
 Almeida, L., Sana, H., Taylor, W., et al. 2017, *A&A*, **598**, A84
 Andrews, J. J., Farr, W. M., Kalogera, V., & Willems, B. 2015, *ApJ*, **801**, 32
 Andrews, J. J., Zezas, A., & Fragos, T. 2018, *ApJS*, **237**, 1
 Arzoumanian, Z., Chernoff, D. F., & Cordes, J. M. 2002, *ApJ*, **568**, 289
 Asplund, M., Grevesse, N., Sauval, A. J., & Scott, P. 2009, *ARA&A*, **47**, 481
 Astropy Collaboration, Price-Whelan, A. M., Sipőcz, B. M., et al. 2018, *AJ*, **156**, 123
 Astropy Collaboration, Robitaille, T. P., Tollerud, E. J., et al. 2013, *A&A*, **558**, A33
 Atri, P., Miller-Jones, J. C. A., Bahramian, A., et al. 2019, *MNRAS*, **489**, 3116
 Babak, S., Taracchini, A., & Buonanno, A. 2017, *PhRvD*, **95**, 024010
 Baibhav, V., Berti, E., Gerosa, D., et al. 2019, *PhRvD*, **100**, 064060
 Banerjee, S., Belczynski, K., Fryer, C. L., et al. 2020, *A&A*, **639**, A41
 Barkat, Z., Rakavy, G., & Sack, N. 1967, *PhRvL*, **18**, 379
 Barrett, J. W., Gaebel, S. M., Neijssel, C. J., et al. 2018, *MNRAS*, **477**, 4685
 Barrett, J. W., Mandel, I., Neijssel, C. J., Stevenson, S., & Vigna-Gomez, A. 2017, in *IAU Symp. 325, Astroinformatics* (Cambridge: Cambridge Univ. Press), 46
 Bavera, S. S., Fragos, T., Qin, Y., et al. 2020, *A&A*, **635**, A97
 Beasor, E. R., & Davies, B. 2018, *MNRAS*, **475**, 55
 Belczynski, K., Bulik, T., Fryer, C. L., et al. 2010, *ApJ*, **714**, 1217
 Belczynski, K., Heger, A., Gladysz, W., et al. 2016a, *A&A*, **594**, A97
 Belczynski, K., Hirschi, R., Kaiser, E. A., et al. 2020a, *ApJ*, **890**, 113
 Belczynski, K., Kalogera, V., & Bulik, T. 2002, *ApJ*, **572**, 407
 Belczynski, K., Kalogera, V., Rasio, F. A., et al. 2008, *ApJS*, **174**, 223
 Belczynski, K., Kalogera, V., Rasio, F. A., Taam, R. E., & Bulik, T. 2007, *ApJ*, **662**, 504
 Belczynski, K., Klencki, J., Fields, C. E., et al. 2020b, *A&A*, **636**, A104
 Belczynski, K., Repetto, S., Holz, D. E., et al. 2016b, *ApJ*, **819**, 108
 Belczynski, K., Romagnolo, A., Olejak, A., et al. 2021, arXiv:2108.10885
 Beniamini, P., & Piran, T. 2016, *MNRAS*, **456**, 4089
 Berger, E. 2014, *ARA&A*, **52**, 43
 Bhattacharya, D., & van den Heuvel, E. P. J. 1991, *PhR*, **203**, 1
 Bisnovatyi-Kogan, G. S. 1993, *A&AT*, **3**, 287
 Blaauw, A. 1961, *BAN*, **15**, 265
 Boco, L., Lapi, A., Chruslinska, M., et al. 2021, *ApJ*, **907**, 110
 Bondi, H., & Hoyle, F. 1944, *MNRAS*, **104**, 273
 Bowman, D. M. 2020, *FrASS*, **7**, 70
 Brandt, N., & Podsiadlowski, P. 1995, *MNRAS*, **274**, 461
 Bray, J. C., & Eldridge, J. J. 2016, *MNRAS*, **461**, 3747
 Bray, J. C., & Eldridge, J. J. 2018, *MNRAS*, **480**, 5657
 Breivik, K., Coughlin, S., Zevin, M., et al. 2020, *ApJ*, **898**, 71
 Briskin, W. F., Benson, J. M., Goss, W. M., & Thorsett, S. E. 2002, *ApJ*, **571**, 906
 Broekgaarden, F. S., & Berger, E. 2021, *ApJL*, **920**, L13
 Broekgaarden, F. S., Berger, E., Neijssel, C. J., et al. 2021a, *MNRAS*, **508**, 5028
 Broekgaarden, F. S., Berger, E., Stevenson, S., et al. 2021b, arXiv:2112.05763
 Broekgaarden, F. S., Justham, S., de Mink, S. E., et al. 2019, *MNRAS*, **490**, 5228
 Brookshaw, L., & Tavani, M. 1993, *ApJ*, **410**, 719
 Brown, G. E. 1995, *ApJ*, **440**, 270

- Burrows, A., & Hayes, J. 1996, *PhRvL*, **76**, 352
- Burrows, A., & Vartanyan, D. 2021, *Natur*, **589**, 29
- Castor, J. I., Abbott, D. C., & Klein, R. I. 1975, *ApJ*, **195**, 157
- Chattopadhyay, D., Stevenson, S., Hurley, J. R., Bailes, M., & Broekgaarden, F. 2021, *MNRAS*, **504**, 3682
- Chattopadhyay, D., Stevenson, S., Hurley, J. R., Rossi, L. J., & Flynn, C. 2020, *MNRAS*, **494**, 1587
- Chevalier, R. A. 1993, *ApJL*, **411**, L33
- Chini, R., Hoffmeister, V., Nasser, A., Stahl, O., & Zinnecker, H. 2012, *MNRAS*, **424**, 1925
- Chiosi, C., & Maeder, A. 1986, *ARA&A*, **24**, 329
- Chruslinska, M., Nelemans, G., & Belczynski, K. 2019, *MNRAS*, **482**, 5012
- Collette, A. 2013, Python and HDF5 (Sebastopol, CA: O'Reilly & Associates)
- Conroy, C., & Kratter, K. M. 2012, *ApJ*, **755**, 123
- de Jager, C., Nieuwenhuijzen, H., & van der Hucht, K. A. 1988, *A&AS*, **72**, 259
- de Kool, M. 1990, *ApJ*, **358**, 189
- De Minkde Mink, S., Langer, N., Izzard, R., Sana, H., & de Koter, A. 2013, *ApJ*, **764**, 166
- Delgado, A. J., & Thomas, H. C. 1981, *A&A*, **96**, 142
- Doherty, C. L., Gil-Pons, P., Siess, L., & Lattanzio, J. C. 2017, *PASA*, **34**, e056
- Dominik, M., Belczynski, K., Fryer, C., et al. 2012, *ApJ*, **759**, 52
- Dominik, M., Belczynski, K., Fryer, C., et al. 2013, *ApJ*, **779**, 72
- Dominik, M., Berté, E., O'Shaughnessy, R., et al. 2015, *ApJ*, **806**, 263
- Donati, J. F., & Landstreet, J. D. 2009, *ARA&A*, **47**, 333
- Dosopoulou, F., & Kalogera, V. 2016, *ApJ*, **825**, 71
- Dray, L. M., & Tout, C. A. 2003, *MNRAS*, **341**, 299
- Duchêne, G., & Kraus, A. 2013, *ARA&A*, **51**, 269
- Dufton, P. L., Langer, N., Dunstall, P. R., et al. 2013, *A&A*, **550**, A109
- Duquennoy, A., & Mayor, M. 1991a, *A&A*, **500**, 337
- Duquennoy, A., & Mayor, M. 1991b, *A&A*, **248**, 485
- Eggleton, P. P. 1983, *ApJ*, **268**, 368
- Eggleton, P. P., Fitchett, M. J., & Tout, C. A. 1989, *ApJ*, **347**, 998
- El-Badry, K., & Rix, H.-W. 2018, *MNRAS*, **480**, 4884
- Eldridge, J. J., Fraser, M., Smartt, S. J., Maund, J. R., & Crockett, R. M. 2013, *MNRAS*, **436**, 774
- Eldridge, J. J., Guo, N. Y., Rodrigues, N., Stanway, E. R., & Xiao, L. 2019a, *PASA*, **36**, e041
- Eldridge, J. J., Stanway, E. R., & Tang, P. N. 2019b, *MNRAS*, **482**, 870
- Eldridge, J. J., Stanway, E. R., Xiao, L., et al. 2017, *PASA*, **34**, e058
- Eldridge, J. J., Xiao, L., Stanway, E. R., Rodrigues, N., & Guo, N. Y. 2018, *PASA*, **35**, 49
- Ertl, T., Janka, H. T., Woosley, S. E., Sukhbold, T., & Ugliano, M. 2016, *ApJ*, **818**, 124
- Farmer, R., Renzo, M., de Mink, S. E., Marchant, P., & Justham, S. 2019, *ApJ*, **887**, 53
- Faucher-Giguere, C.-A., & Kaspi, V. M. 2006, *ApJ*, **643**, 332
- Finn, L. S., & Chernoff, D. F. 1993, *PhRvD*, **47**, 2198
- Fowler, W. A., & Hoyle, F. 1964, *ApJS*, **9**, 201
- Fraleigh, G. S. 1968, *Ap&SS*, **2**, 96
- Friend, D. B., & Abbott, D. C. 1986, *ApJ*, **311**, 701
- Fryer, C. L., Belczynski, K., Wiktorowicz, G., et al. 2012, *ApJ*, **749**, 91
- Furlong, M., Bower, R. G., Theuns, T., et al. 2015, *MNRAS*, **450**, 4486
- Galassi, M., Davies, J., Theiler, J., et al. 2002, GNU Scientific Library (Göteborg: Network Theory Limited)
- Ge, H., Webbink, R. F., Chen, X., & Han, Z. 2015, *ApJ*, **812**, 40
- Geller, A. M., Hurley, J. R., & Mathieu, R. D. 2013, *AJ*, **145**, 8
- Gessner, A., & Janka, H.-T. 2018, *ApJ*, **865**, 61
- Giacobbo, N., & Mapelli, M. 2018, *MNRAS*, **480**, 2011
- Giacobbo, N., & Mapelli, M. 2020, *ApJ*, **891**, 141
- Giacobbo, N., Mapelli, M., & Spera, M. 2018, *MNRAS*, **474**, 2959
- Götberg, Y., de Mink, S. E., Groh, J. H., Leitherer, C., & Norman, C. 2019, *A&A*, **629**, A134
- Götberg, Y., de Mink, S. E., McQuinn, M., et al. 2020, *A&A*, **634**, A134
- Gunn, J. E., & Ostriker, J. P. 1970, *ApJ*, **160**, 979
- Hamann, W.-R., & Koesterke, L. 1998, *A&A*, **335**, 1003
- Hannam, M., Schmidt, P., Bohé, A., et al. 2014, *PhRvL*, **113**, 151101
- Hansen, B. M. S., & Phinney, E. S. 1997, *MNRAS*, **291**, 569
- Harris, C. R., Millman, K. J., van der Walt, S. J., et al. 2020, *Natur*, **585**, 357
- Heger, A., Langer, N., & Woosley, S. E. 2000, *ApJ*, **528**, 368
- Heggie, D. C. 1975, *MNRAS*, **173**, 729
- Hild, S., Abernathy, M., Acernese, F., et al. 2011, *CQGra*, **28**, 094013
- Hills, J. G. 1983, *ApJ*, **267**, 322
- Hirai, R., & Mandel, I. 2021, *PASA*, **38**, e056
- Hjellming, M. S., & Webbink, R. F. 1987, *ApJ*, **318**, 794
- Hobbs, G., Lorimer, D. R., Lyne, A. G., & Kramer, M. 2005, *MNRAS*, **360**, 974
- Höfner, S., & Olofsson, H. 2018, *A&ARv*, **26**, 1
- Hogg, D. W. 1999, arXiv:astro-ph/9905116
- Howitt, G., Stevenson, S., Vigna-Gómez, A. r., et al. 2020, *MNRAS*, **492**, 3229
- Hoyle, F., & Lyttleton, R. A. 1939, *PCPS*, **35**, 405
- Huang, S. S. 1956, *AJ*, **61**, 49
- Huang, S.-S. 1963, *ApJ*, **138**, 471
- Humphreys, R. M., & Davidson, K. 1994, *PASP*, **106**, 1025
- Hunter, J. D. 2007, *CSE*, **9**, 90
- Hurley, J. R., Pols, O. R., & Tout, C. A. 2000, *MNRAS*, **315**, 543
- Hurley, J. R., Tout, C. A., & Pols, O. R. 2002, *MNRAS*, **329**, 897
- Husa, S., Khan, S., Hannam, M., et al. 2016, *PhRvD*, **93**, 044006
- Ivanova, N., Heinke, C. O., Rasio, F. A., Belczynski, K., & Fregeau, J. M. 2008, *MNRAS*, **386**, 553
- Ivanova, N., Justham, S., Chen, X., et al. 2013, *A&ARv*, **21**, 59
- Ivanova, N., & Taam, R. E. 2004, *ApJ*, **601**, 1058
- Izzard, R. G., Dray, L. M., Karakas, A. I., Lugaro, M., & Tout, C. A. 2006, *A&A*, **460**, 565
- Izzard, R. G., Glebbeek, E., Stancliffe, R. J., & Pols, O. R. 2009, *A&A*, **508**, 1359
- Izzard, R. G., Tout, C. A., Karakas, A. I., & Pols, O. R. 2004, *MNRAS*, **350**, 407
- Janka, H. T. 2013, *MNRAS*, **434**, 1355
- Janka, H.-T., & Müller, E. 1994, *A&A*, **290**, 496
- Johnston, S., Hobbs, G., Vigeland, S., et al. 2005, *MNRAS*, **364**, 1397
- Kalogera, V. 1996, *ApJ*, **471**, 352
- Khan, S., Husa, S., Hannam, M., et al. 2016, *PhRvD*, **93**, 044007
- Kiel, P., Hurley, J., Bailes, M., & Murray, J. 2008, *MNRAS*, **388**, 393
- Klencki, J., Moe, M., Gladysz, W., et al. 2018, *A&A*, **619**, A77
- Klencki, J., Nelemans, G., Istrate, A. G., & Chruslinska, M. 2021, *A&A*, **645**, A54
- Kluwyer, T., Ragan-Kelley, B., Pérez, F., et al. 2016, Positioning and Power in Academic Publishing: Players, Agents and Agendas (Amsterdam: IOS Press), 87
- Kobulnicky, H. A., Kiminki, D. C., Lundquist, M. J., et al. 2014, *ApJS*, **213**, 34
- Kozyreva, A., Blinnikov, S., Langer, N., & Yoon, S. C. 2014a, *A&A*, **565**, A70
- Kozyreva, A., Gilmer, M., Hirschi, R., et al. 2017, *MNRAS*, **464**, 2854
- Kozyreva, A., Yoon, S. C., & Langer, N. 2014b, *A&A*, **566**, A146
- Kroupa, P. 2001, *MNRAS*, **322**, 231
- Kruckow, M. U., Tauris, T. M., Langer, N., et al. 2016, *A&A*, **596**, A58
- Kudritzki, R. P., Pauldrach, A., Puls, J., & Abbott, D. C. 1989, *A&A*, **219**, 205
- Kudritzki, R. P., & Reimers, D. 1978, *A&A*, **70**, 227
- Lai, D., Chernoff, D. F., & Cordes, J. M. 2001, *ApJ*, **549**, 1111
- Langer, N. 1992, *A&A*, **265**, L17
- Langer, N. 2012, *ARA&A*, **50**, 107
- Langer, N., & Norman, C. A. 2006, *ApJL*, **638**, L63
- Lattimer, J. M., & Schutz, B. F. 2005, *ApJ*, **629**, 979
- Lau, M. Y. M., Mandel, I., Vigna-Gómez, A., et al. 2020, *MNRAS*, **492**, 3061
- Leung, S.-C., Nomoto, K., & Blinnikov, S. 2019, *ApJ*, **887**, 72
- LIGO Scientific Collaboration 2018, LIGO Algorithm Library—LALSuite, Free Software (GPL), doi:10.7935/GT1W-FZ16
- Lin, L., Bingham, D., Broekgaarden, F., & Mandel, I. 2021, arXiv:2106.01552
- Lipunov, V. M., Ozernoy, L. M., Popov, S. B., Postnov, K. A., & Prokhorov, M. E. 1996a, *ApJ*, **466**, 234
- Lipunov, V. M., Postnov, K. A., & Prokhorov, M. E. 1996b, *A&A*, **310**, 489
- Lipunov, V. M., Postnov, K. A., Prokhorov, M. E., & Bogomazov, A. I. 2009, *ARep*, **53**, 915
- Loveridge, A. J., van der Sluis, M. V., & Kalogera, V. 2011, *ApJ*, **743**, 49
- Lyne, A. G., & Lorimer, D. R. 1994, *Natur*, **369**, 127
- Ma, X., Hopkins, P. F., Faucher-Giguère, C.-A., et al. 2016a, *MNRAS*, **456**, 2140
- Ma, X., Hopkins, P. F., Kasen, D., et al. 2016b, *MNRAS*, **459**, 3614
- MacLeod, M., & Ramirez-Ruiz, E. 2015, *ApJL*, **798**, L19
- Madau, P., & Dickinson, M. 2014, *ARA&A*, **52**, 415
- Madau, P., & Fragos, T. 2017, *ApJ*, **840**, 39
- Maeder, A. 1987, *A&A*, **178**, 159
- Maeder, A., & Meynet, G. 2000, *ARA&A*, **38**, 143
- Mandel, I. 2016, *MNRAS*, **456**, 578
- Mandel, I., & Broekgaarden, F. S. 2021, arXiv:2107.14239
- Mandel, I., & de Mink, S. E. 2016, *MNRAS*, **458**, 2634
- Mandel, I., & Farmer, A. 2018, arXiv:1806.05820
- Mandel, I., & Müller, B. 2020, *MNRAS*, **499**, 3214
- Mandel, I., Müller, B., Riley, J., et al. 2021, *MNRAS*, **500**, 1380

- Marchant, P., Langer, N., Podsiadlowski, P., Tauris, T. M., & Moriya, T. J. 2016, *A&A*, **588**, A50
- Marchant, P., Renzo, M., Farmer, R., et al. 2019, *ApJ*, **882**, 36
- Massevitch, A., & Yungelson, L. 1975, *MmSAI*, **46**, 217
- Mestel, L. 1952, *MNRAS*, **112**, 583
- Miller-Jones, J. C. A., Bahramian, A., Orosz, J. A., et al. 2021, *Sci*, **371**, 1046
- Miyaji, S., Nomoto, K., Yokoi, K., & Sugimoto, D. 1980, *PASJ*, **32**, 303
- Moe, M., & Di Stefano, R. 2017, *ApJS*, **230**, 15
- Mohamed, S., & Podsiadlowski, P. 2007, in ASP Conf. Ser. 372, 15th European Workshop on White Dwarfs, ed. R. Napiwotzki & M. R. Burleigh (San Francisco, CA: ASP), 397
- Mokiem, M. R., de Koter, A., Vink, J. S., et al. 2007, *A&A*, **473**, 603
- Moriya, T. J., Mazzali, P. A., Tominaga, N., et al. 2017, *MNRAS*, **466**, 2085
- Müller, B. 2020, *LRCA*, **6**, 3
- Müller, B., Gay, D. W., Heger, A., Tauris, T. M., & Sim, S. A. 2018, *MNRAS*, **479**, 3675
- Müller, B., Heger, A., Liptai, D., & Cameron, J. B. 2016, *MNRAS*, **460**, 742
- Müller, B., Tauris, T. M., Heger, A., et al. 2019, *MNRAS*, **484**, 3307
- Nagakura, H., Sumiyoshi, K., & Yamada, S. 2019, *ApJL*, **880**, L28
- Nakamura, K., Takiwaki, T., Kuroda, T., & Kotake, K. 2015, *PASJ*, **67**, 107
- Neijssel, C. J., Vigna-Gómez, A., Stevenson, S., et al. 2019, *MNRAS*, **490**, 3740
- Neijssel, C. J., Vinciguerra, S., Vigna-Gómez, A., et al. 2021, *ApJ*, **908**, 118
- Nelemans, G., Yungelson, L. R., Portegies Zwart, S. F., & Verbunt, F. 2001, *A&A*, **365**, 491
- Neo, S., Miyaji, S., Nomoto, K., & Sugimoto, D. 1977, *PASJ*, **29**, 249
- Nieuwenhuijzen, H., & de Jager, C. 1990, *A&A*, **231**, 134
- Nomoto, K. 1984, *ApJ*, **277**, 791
- Nomoto, K. 1987, *ApJ*, **322**, 206
- Nomoto, K., & Kondo, Y. 1991, *ApJL*, **367**, L19
- Noutsos, A., Kramer, M., Carr, P., & Johnston, S. 2012, *MNRAS*, **423**, 2736
- Öpik, E. 1924, *PTarO*, **25**, 1
- Ošowski, S., Bulik, T., Gondek-Rosińska, D., & Belczyński, K. 2011, *MNRAS*, **413**, 461
- Paczynski, B. 1976, in IAU Symp. 73, Structure and Evolution of Close Binary Systems, ed. P. Eggleton, S. Mitton, & J. Whelan (Dordrecht: D. Reidel), 75
- Paczynski, B., & Sienkiewicz, R. 1972, *AcA*, **22**, 73
- Pan, Y., Buonanno, A., Taracchini, A., et al. 2014, *PhRvD*, **89**, 084006
- Panther, B., Heavens, A. F., & Jimenez, R. 2004, *MNRAS*, **355**, 764
- Pérez, F., & Granger, B. E. 2007, *CSE*, **9**, 21
- Peters, P. C. 1964, *PhRv*, **136**, 1224
- Pfahl, E., Rappaport, S., & Podsiadlowski, P. 2002a, *ApJL*, **571**, L37
- Pfahl, E., Rappaport, S., & Podsiadlowski, P. 2002b, *ApJ*, **573**, 283
- Planck Collaboration, Ade, P. A. R., Aghanim, N., et al. 2016, *A&A*, **594**, A13
- Podsiadlowski, P. 2001, in ASP Conf. Ser. 229, Common-envelope Evolution and Stellar Mergers, ed. P. Podsiadlowski et al. (San Francisco, CA: ASP), 239
- Podsiadlowski, P. 2010, *NewAR*, **54**, 39
- Podsiadlowski, P., Joss, P. C., & Hsu, J. J. L. 1992, *ApJ*, **391**, 246
- Podsiadlowski, P., Langer, N., Poelarends, A. J. T., et al. 2004, *ApJ*, **612**, 1044
- Pols, O. R., Schröder, K.-P., Hurley, J. R., Tout, C. A., & Eggleton, P. P. 1998, *MNRAS*, **298**, 525
- Portegies Zwart, S. F., & Verbunt, F. 1996, *A&A*, **309**, 179
- Portegies Zwart, S. F., & Yungelson, L. R. 1998, *A&A*, **332**, 173
- Postnov, K. A., & Yungelson, L. R. 2014, *LRR*, **17**, 3
- Ramírez-Agudelo, O. H., Simón-Díaz, S., Sana, H., et al. 2013, *A&A*, **560**, A29
- Remillard, R. A., & McClintock, J. E. 2006, *ARA&A*, **44**, 49
- Renzo, M., Farmer, R., Justham, S., et al. 2020, *A&A*, **640**, A56
- Renzo, M., Ott, C. D., Shore, S. N., & de Mink, S. E. 2017, *A&A*, **603**, A118
- Repetto, S., Igoshev, A. P., & Nelemans, G. 2017, *MNRAS*, **467**, 298
- Riley, J., Mandel, I., Marchant, P., et al. 2021, *MNRAS*, **505**, 663
- Rosdahl, J., Katz, H., Blaizot, J., et al. 2018, *MNRAS*, **479**, 994
- Salpeter, E. E. 1955, *ApJ*, **121**, 161
- Sana, H. 2017, in IAU Symp. 329, The Lives and Death-Throes of Massive Stars, ed. J. J. Eldridge et al. (Cambridge: Cambridge Univ. Press), 110
- Sana, H., de Mink, S. E., de Koter, A., et al. 2012, *Sci*, **337**, 444
- Sana, H., Le Bouquin, J. B., Lacour, S., et al. 2014, *ApJS*, **215**, 15
- Sander, A. A. C., Vink, J. S., & Hamann, W. R. 2020, *MNRAS*, **491**, 4406
- Savaglio, S., Glazebrook, K., Le Borgne, D., et al. 2005, *ApJ*, **635**, 260
- Schneider, F. R. N., Izzard, R. G., Langer, N., & de Mink, S. E. 2015, *ApJ*, **805**, 20
- Schneider, F. R. N., Podsiadlowski, P., & Müller, B. 2021, *A&A*, **645**, A5
- Schröder, S. L., MacLeod, M., Loeb, A., Vigna-Gómez, A., & Mandel, I. 2020, *ApJ*, **892**, 13
- Schröder, S. L., MacLeod, M., Ramirez-Ruiz, E., et al. 2021, arXiv:2107.09675
- Schwab, J., Podsiadlowski, P., & Rappaport, S. 2010, *ApJ*, **719**, 722
- Smith, N. 2014, *ARA&A*, **52**, 487
- Soberman, G. E., Phinney, E. S., & van den Heuvel, E. P. J. 1997, *A&A*, **327**, 620
- Socrates, A., Blaes, O., Hungerford, A., & Fryer, C. L. 2005, *ApJ*, **632**, 531
- Spera, M., & Mapelli, M. 2017, *MNRAS*, **470**, 4739
- Stevenson, S., Sampson, M., Powell, J., et al. 2019, *ApJ*, **882**, 121
- Stevenson, S., Vigna-Gómez, A., Mandel, I., et al. 2017, *NatCo*, **8**, 14906
- Strolger, L.-G., Riess, A. G., Dahlen, T., et al. 2004, *ApJ*, **613**, 200
- Sukhbold, T., & Adams, S. 2020, *MNRAS*, **492**, 2578
- Sukhbold, T., & Woosley, S. 2014, *ApJ*, **783**, 10
- Suwa, Y., Yoshida, T., Shibata, M., Umeda, H., & Takahashi, K. 2015, *MNRAS*, **454**, 3073
- Taam, R. E., & Sandquist, E. L. 2000, *ARA&A*, **38**, 113
- Takahashi, K. 2018, *ApJ*, **863**, 153
- Talon, S., Zahn, J.-P., Maeder, A., & Meynet, G. 1997, *A&A*, **322**, 209
- Tauris, T. M., Kramer, M., Freire, P. C. C., et al. 2017, *ApJ*, **846**, 170
- Tauris, T. M., Langer, N., Moriya, T. J., et al. 2013, *ApJL*, **778**, L23
- Tauris, T. M., Langer, N., & Podsiadlowski, P. 2015, *MNRAS*, **451**, 2123
- Tauris, T. M., & Takens, R. J. 1998, *A&A*, **330**, 1047
- Tauris, T. M., & van den Heuvel, E. P. J. 2006, in Compact Stellar X-ray Sources, ed. W. Lewin & M. van der Klis (Cambridge: Cambridge Univ. Press), 623
- Taylor, S. R., & Gerosa, D. 2018, *PhRvD*, **98**, 083017
- Team COMPAS 2022, *JOSS*, **7**, 3838
- Timmes, F. X., Woosley, S. E., & Weaver, T. A. 1996, *ApJ*, **457**, 834
- Toonen, S., Nelemans, G., & Portegies Zwart, S. 2012, *A&A*, **546**, A70
- Tout, C. A., Aarseth, S. J., Pols, O. R., & Eggleton, P. P. 1997, *MNRAS*, **291**, 732
- Tout, C. A., Pols, O. R., Eggleton, P. P., & Han, Z. 1996, *MNRAS*, **281**, 257
- Tutukov, A., & Yungelson, L. 1996, *MNRAS*, **280**, 1035
- Ugliano, M., Janka, H.-T., Marek, A., & Arcones, A. 2012, *ApJ*, **757**, 69
- van den Heuvel, E. P. J. 1976, in IAU Symp. 73, Structure and Evolution of Close Binary Systems, ed. P. Eggleton, S. Mitton, & J. Whelan (Cambridge: Cambridge Univ. Press), 35
- van Rossum, G. 1995, Python Tutorial, Tech. Rep., CS-R9526 (Amsterdam: Centrum voor Wiskunde en Informatica)
- van Son, L., de Mink, S., Broekgaarden, F., et al. 2020, *ApJ*, **897**, 100
- van Son, L. A. C., de Mink, S. E., Callister, T., et al. 2021, arXiv:2110.01634
- Vassiliadis, E., & Wood, P. R. 1993, *ApJ*, **413**, 641
- Verbunt, F., Igoshev, A., & Cator, E. 2017, *A&A*, **608**, A57
- Vick, M., & Lai, D. 2020, *MNRAS*, **496**, 3767
- Vigna-Gómez, A., MacLeod, M., Neijssel, C. J., et al. 2020, *PASA*, **37**, e038
- Vigna-Gómez, A., Neijssel, C. J., Stevenson, S., et al. 2018, *MNRAS*, **481**, 4009
- Vigna-Gómez, A., Toonen, S., Ramirez-Ruiz, E., et al. 2021, *ApJL*, **907**, L19
- Vinciguerra, S., Neijssel, C. J., Vigna-Gómez, A., et al. 2020, *MNRAS*, **498**, 4705
- Vink, J. S., & de Koter, A. 2005, *A&A*, **442**, 587
- Vink, J. S., de Koter, A., & Lamers, H. J. G. L. M. 2000, *A&A*, **362**, 295
- Vink, J. S., de Koter, A., & Lamers, H. J. G. L. M. 2001, *A&A*, **369**, 574
- Virtanen, P., Gommers, R., Oliphant, T. E., et al. 2020, *NatMe*, **17**, 261
- Waskom, M., Gelbart, M., Botvinnik, O., et al. 2020, mwaskom/seaborn: v0.11.2 (August 2021), Zenodo, doi:10.5281/zenodo.592845
- Webbink, R. F. 1984, *ApJ*, **277**, 355
- Willcox, R., Mandel, I., Thrane, E., et al. 2021, *ApJL*, **920**, L37
- Wongwanarat, A., Janka, H. T., & Mueller, E. 2013, *A&A*, **552**, A126
- Woods, T. E., Ivanova, N., van der Sluis, M. V., & Chaichenets, S. 2012, *ApJ*, **744**, 12
- Woosley, S., & Heger, A. 2007, *PhR*, **442**, 269
- Woosley, S. E. 1987, in IAU Symp. 125, The Origin and Evolution of Neutron Stars, ed. D. J. Helfand & J. H. Huang (Dordrecht: D. Reidel), 255
- Woosley, S. E. 2017, *ApJ*, **836**, 244
- Woosley, S. E. 2019, *ApJ*, **878**, 49
- Woosley, S. E., & Bloom, J. S. 2006, *ARA&A*, **44**, 507
- Woosley, S. E., Heger, A., & Weaver, T. A. 2002, *RvMP*, **74**, 1015
- Xu, X.-J., & Li, X.-D. 2010a, *ApJ*, **716**, 114
- Xu, X.-J., & Li, X.-D. 2010b, *ApJ*, **722**, 1985

Yao, J., Zhu, W., Manchester, R. N., et al. 2021, [NatAs](#), **5**, 788

Ye, C. S., Kremer, K., Chatterjee, S., Rodriguez, C. L., & Rasio, F. A. 2019, [ApJ](#), **877**, 122

Yoon, S.-C., Chun, W., Tolstov, A., Blinnikov, S., & Dessart, L. 2019, [ApJ](#), **872**, 174

Yoon, S.-C., Dessart, L., & Clocchiatti, A. 2017, [ApJ](#), **840**, 10

Yoshida, T., Umeda, H., Maeda, K., & Ishii, T. 2016, [MNRAS](#), **457**, 351

Zapartas, E., de Mink, S. E., Justham, S., et al. 2019, [A&A](#), **631**, A5

Zapartas, E., de Mink, S. E., Justham, S., et al. 2021, [A&A](#), **645**, A6